A Three-Dimensional Cloud Model Based on the Vector Vorticity Equation

by

Joon-Hee Jung
Department of Atmospheric Science, Colorado State University, Colorado,

Akio Arakawa
Department of Atmospheric and Oceanic Sciences, UCLA, California

Research supported by
the U. S. Department of Energy
under Grant number DE-FG02-02ER63370 to Colorado State Univ.
and CSU Contract G-3816-3 to UCLA
and by the National Aeronautics and Space Administration
under Grant number NNG04GA76G to UCLA

Department of Atmospheric Science
Colorado State University
Fort Collins, Colorado

November 2005
(*Revised, April 2007*)

Atmospheric Science Paper No. 762

A Three-Dimensional Cloud Model Based on the Vector Vorticity Equation

Joon-Hee Jung
Department of Atmospheric Science, Colorado State University, Colorado, USA,

Akio Arakawa
Department of Atmospheric and Oceanic Sciences, UCLA, California, USA

FOREWORD

This technical report presents a detailed description of a new three-dimensional cloud model we have developed. Since the 1970s, a number of three-dimensional cloud models were developed. Practically all of them are built on the dynamical framework of the momentum equation. Our model uses the vector vorticity equation instead, in which the pressure gradient force is eliminated. Since the pressure field is passive to the anelastic motion, the relevant dynamical processes are more explicitly expressed in this way and, therefore, diagnosis and interpretation of the model results can be more straightforward. The use of the vorticity equation is also advantageous from the viewpoint of computational design because computational requirements on the key dynamical processes can be more directly implemented.

Table of Contents

1. Introduction

In the process of cloud modeling during the last decades, it was clearly realized that one- and two-dimensional cloud models are usually not capable of realistically simulating the complex behavior of convective systems. A number of three-dimensional cloud models were developed to simulate the structure, intensity and movement of convective clouds. For example, Steiner (1973) demonstrated the need of three-dimensional models to simulate convection by comparing the development of a shallow, non-precipitating cumulus cloud in two-dimensional and three-dimensional domains. Wihelmson (1974), Miler and Pearce (1974), Pastushkov (1975), Moncrieff and Miller (1976), and Schlesinger (1978) simulated deep precipitating convection in a three-dimensional domain. Wihelmson and Klemp (1978) simulated details of the dynamics of convective storms such as their occasional splitting. They found that the splitting is the direct result of precipitation and the magnitude of the low-level shear affects the storm development.

Since the 70's, three-dimensional cloud models have been successfully used in simulating observed characteristics of supercells and multicell storms in midlatitudes (Wihelmson and Klemp, 1981; Wihelmson and Chen, 1982) and convection in the tropics (Turpeinen and Yau, 1981; Simpson *et al*., 1982). With the help of increasingly powerful computers, models have also been used to simulate the development of an ensemble of cumulus clouds with random heating (Tao and Soong, 1986) or with a surface layer model that incorporates observed heat and moisture fluxes (Smolarkiewicz and Clark, 1985). Donner *et al*. (1999) simulated deep convection and its associated mesoscale circulations observed during the GARP Atlantic Tropical Experiment (GATE).

Considerable progress has also been made in microphysical parameterizations in three-dimensional cloud models. In the 70s and 80s, three-dimensional severe storm simulations were carried out usually with simple Kessler-type parameterizations. The need of more detailed treatment of microphysical processes, however, was recognized. Lin *et al*. (1983) developed a three-class ice scheme that includes many microphysical processes. Lord *et al*.

(1984) modified the ice scheme of Lin *et al.* by adjusting some of the hydrometeor densities and intercept parameters for better simulations of hurricanes. Cotton *et al.* (1986) extended their two-class ice scheme to three classes. To evaluate the performance of several ice parameterizations, McCumber *et al.* (1991) simulated tropical squall-type and nonsquall-type convections using a three-dimensional cloud model. Johnson *et al.* (1993) showed that the inclusion of ice alters the dynamics, kinematics, thermodynamics, and distributions of water in the simulated supercell storm especially at the lower levels.

Many tests have been carried out to systematically compare two- and three-dimensional cloud models (e.g. Tao and Soong, 1986; Tao *et al*., 1987; Grabowski *et al*., 1998; Redelsperger *et al.* 2000, Khairoutdinov and Randall, 2003). These studies reported that downdrafts and momentum transport properties were significantly different between the two- and three-dimensional simulations although many convective statistics such as precipitation and relative humidity could be similar. In particular, Redelsperger *et al.* (2000) pointed out that the evolution of the mean wind profile was in the sense of decreasing the shear in the three-dimensional simulations, but the two-dimensional simulations were unable to produce this behavior. Mapes and Wu (2001), on the other hand, showed that the convective momentum transports from two- and three-dimensional simulations of GATE convective systems are qualitatively similar in pattern. Zhang and Wu (2003) interpreted this result as a consequence of the strong nudging of the domain-averaged wind profiles toward observed used in the two-dimensional simulation, indicating that the feedback to the mean wind by the convective momentum transport amplifies the difference between the two- and three-dimensional simulations.

The three-dimensional cloud models can be classified into two types: one is based on the anelastic system of equations and the other on the fully compressible system of equations. In the anelastic models, the pressure perturbation is calculated for a given motion field using a diagnostic elliptic equation, of which boundary condition produces computational complications when it is applied to flow over a complex terrain. Such complications can be eliminated in the fully compressible models. However, sound waves are retained in the system so that they must be appropriately handled computationally. A

technique called "splitting", in which the sound wave modes are solved separately using a shorter time step than elsewhere in the model, is widely used in many compressible models (e.g., Klemp and Wihelmson, 1978).

Whether they are anelastic or fully compressible, practically all of the three-dimensional cloud models developed so far view the dynamics of convection mainly in terms of the pressure gradient and buoyancy forces in the context of the momentum equation. The presence of vortical motions association with convective clouds, however, can lead us to examine the motions using the vorticity equation, which eliminates the pressure gradient force and thus more directly addresses the motion in terms of the buoyancy source. In two-dimensional modeling, this advantage of the voricity equation can be easily taken. Two-dimensional vorticity equation models have been extensively applied to a variety of cloud regimes including stratocumulus, altocumulus, cumulo-nimbus and cirrus clouds (see, for example, Krueger 2000). In three-dimensional cloud modeling, on the contrary, to our knowledge no attempt has been made to use the vorticity equation as a dynamical core, although the vertical vorticity fields associated with deep convective clouds were *diagnostically* investigated by many authors (Schlesinger, 1980; Cho and Clark, 1981; Rotunno, 1981; Klemp *et al*., 1981).

In this report, we present a three-dimensional anelastic cloud model based on the vorticity equation. The anelastic equations remain a good approximation for the governing dynamics of cumulus convection and, together with the use of the vorticity equation, express relevant dynamical processes more explicitly. Thus the diagnosis of model results can be more straightforward and consistent with the prognosis. In the anelastic vorticity dynamics, for example, the cumulus momentum transport problem can be more simply viewed from the point of view of vorticity fluxes, while it is quite complicated in the standard momentum dynamics due to the existence of the pressure perturbation. Predicting vorticity is advantageous especially for the three-dimensional case because the twisting effect of vector vorticity, which plays key roles in the dynamics of three-dimensional convective motions, can be explicitly formulated. Also, when the vorticity fields are predicted, the three-dimensional elliptic equation necessary for anelastic motions can be solved for vertical velocity rather than for pressure,

as we show later in this report. This drastically simplifies the problem of boundary condition at the surface of complex terrains. The use of the vorticity equation is also advantageous from the viewpoint of computational design because computational requirements on the key nonlinear dynamical processes, such as those on enstrophy cascade under advection processes, can be more directly implemented.

Although our initial motivation for developing this model was to study cumulus clouds organized on the mesoscale, we plan to include larger scales in future by applying the model to a larger domain, even to the global domain eventually. In the course of this development, we may attempt to include the effect of full compressibility at least approximately, which can be important for deep planetary-scale motions, while maintaining the basic structure of the model. Here we note that from the point of view of the dispersion properties of inertia-gravity waves, the use of the vorticity and divergence equation is more advantageous than the use of the momentum equation (Randall 1994).

The main purpose of this report is to demonstrate the computational performance of the new model, as well as to gain better understanding of some basic convective processes from the viewpoint of vorticity dynamics. For this reason, idealized experiments simulating thermals in various conditions are carried out as well as those for more complicated cloud systems.

In sections 2 and 3, the basic governing equations of dynamical framework and their spatial discretizations are presented. The physical parameterizations used in the model are briefly described in section 4. Additional aspects of the discretization of the model are presented in section 5. In sections 6 and 7, we present the results of idealized experiments without physics and those of ensemble clouds with full physics. Finally, a summary is presented in section 8.

2. **Dynamical framework**

a. Basic governing equations

An anelastic system of the continuity and momentum equations is given by Lipps and Hemler (1982). With the Cartesian coordinates, theses equations may be written as

$$\frac{\partial}{\partial x}(\rho_0 u)+\frac{\partial}{\partial y}(\rho_0 v)+\frac{\partial}{\partial z}(\rho_0 w)=0\,, \tag{2.1}$$

$$\frac{du}{dt}-fv=-\frac{\partial}{\partial x}\left(c_p\theta_{v0}\pi'\right)-\frac{\partial}{\partial x}\left(\overline{u''u''}\right)-\frac{\partial}{\partial y}\left(\overline{u''v''}\right)-\frac{1}{\rho_0}\frac{\partial}{\partial z}\left(\rho_0\overline{u''w''}\right), \tag{2.2}$$

$$\frac{dv}{dt}+fu=-\frac{\partial}{\partial y}\left(c_p\theta_{v0}\pi'\right)-\frac{\partial}{\partial x}\left(\overline{u''v''}\right)-\frac{\partial}{\partial y}\left(\overline{v''v''}\right)-\frac{1}{\rho_0}\frac{\partial}{\partial z}\left(\rho_0\overline{v''w''}\right), \tag{2.3}$$

$$\begin{aligned}\frac{dw}{dt}=&-\frac{\partial}{\partial z}\left(c_p\theta_{v0}\pi'\right)+g\left(\frac{\theta'}{\theta_0}+0.61q_v-q_c-q_i-q_r-q_s-q_g\right)\\&-\frac{\partial}{\partial x}\left(\overline{u''w''}\right)-\frac{\partial}{\partial y}\left(\overline{v''w''}\right)-\frac{1}{\rho_0}\frac{\partial}{\partial z}\left(\rho_0\overline{w''w''}\right),\end{aligned} \tag{2.4}$$

Here u, v, and w are the x-, y-, and z-components of velocity, respectively, ρ the density, f the Coriolis parameter, g the gravitational acceleration, θ the potential temperature, θ_v the virtual potential temperature defined by $\theta_v \equiv \theta(1+0.61q_v)$, q the mixing ratio of water vapor (v), cloud water (c), cloud ice (i), rain water (r), snow (s) or graupel (g). In theses equations, variables with a subscript 0 refer to the hydrostatic reference state, which varies in z only. The Coliolis force is simplified by omitting its component that depends on the cosine of latitude. A single prime indicates the departure from the reference state and double primes indicate turbulence-scale velocity components. The nondimensional pressure π is given by $\pi=(p/p_{00})^{R/c_p}$, where p is the pressure, p_{00} a constant reference pressure, R the gas constant for dry air and c_p the specific heat of dry air. The operator d/dt denotes the material time derivative, which can be expressed for a quantity A as

$$\frac{dA}{dt} = \frac{\partial A}{\partial t} + u\frac{\partial A}{\partial x} + v\frac{\partial A}{\partial y} + w\frac{\partial A}{\partial z}. \tag{2.5}$$

In the model, the vorticity equation is used instead of the momentum equation. We first define the x-, y-, and z-components of vorticity by

$$\rho_0\xi \equiv \frac{\partial w}{\partial y} - \frac{\partial v}{\partial z},\ \rho_0\eta \equiv \frac{\partial u}{\partial z} - \frac{\partial w}{\partial x},\ \rho_0\zeta \equiv \frac{\partial v}{\partial x} - \frac{\partial u}{\partial y}, \tag{2.6}$$

respectively. (In this definition, the factor ρ_0 is used to include the effect of expansion on vortices as density changes.) Equations (2.6) identically satisfy the nondivergence of the three-dimensional vorticity vector given by

$$\frac{\partial}{\partial x}(\rho_0\xi) + \frac{\partial}{\partial y}(\rho_0\eta) + \frac{\partial}{\partial z}(\rho_0\zeta) = 0. \tag{2.7}$$

From (2.2), (2.3) and (2.4), the x-, y-, and z-components of the vorticity equation can be derived as

$$\rho_0\frac{\partial \xi}{\partial t} = -\left[\frac{\partial}{\partial y}(\rho_0 v\xi) + \frac{\partial}{\partial z}(\rho_0 w\xi)\right] + \frac{\partial}{\partial y}(\rho_0 u\eta) + \frac{\partial}{\partial z}(\rho_0 u\zeta) + f\frac{\partial u}{\partial z} + \frac{\partial B}{\partial y} + \frac{\partial F_w}{\partial y} - \frac{\partial F_v}{\partial z}, \tag{2.8}$$

$$\rho_0\frac{\partial \eta}{\partial t} = -\left[\frac{\partial}{\partial x}(\rho_0 u\eta) + \frac{\partial}{\partial z}(\rho_0 w\eta)\right] + \frac{\partial}{\partial x}(\rho_0 v\xi) + \frac{\partial}{\partial z}(\rho_0 v\zeta) + f\frac{\partial v}{\partial z} - \frac{\partial B}{\partial x} - \frac{\partial F_w}{\partial x} + \frac{\partial F_u}{\partial z}, \tag{2.9}$$

$$\rho_0\frac{\partial \zeta}{\partial t} = -\left[\frac{\partial}{\partial x}(\rho_0 u\zeta) + \frac{\partial}{\partial y}(\rho_0 v\zeta)\right] + \frac{\partial}{\partial x}(\rho_0 w\xi) + \frac{\partial}{\partial y}(\rho_0 w\eta) - f\left(\frac{\partial u}{\partial x} + \frac{\partial v}{\partial y}\right) + \frac{\partial F_v}{\partial x} - \frac{\partial F_u}{\partial y}, \tag{2.10}$$

where B is the buoyancy given by $g\left(\theta'/\theta_0 + 0.61q_v - q_c - q_i - q_r - q_s - q_g\right)$ and F_u, F_v and F_w are the turbulent flux convergence terms in the right-hand-side of (2.2), (2.3) and (2.4), respectively. Note that the pressure gradient force is eliminated in this system.

The thermodynamic equation is given by

$$c_p\pi_0\frac{d\theta}{dt}+L\frac{dq_v}{dt}=-\frac{1}{\rho_0}\left[\frac{\partial}{\partial x}\left(\rho_0\overline{u''h''}\right)+\frac{\partial}{\partial y}\left(\rho_0\overline{v''h''}\right)+\frac{\partial}{\partial z}\left(\rho_0\overline{w''h''}\right)\right]+Q_R+Q_A, \quad (2.11)$$

where h is the moist static energy defined by $h\equiv c_p\pi_0\theta+Lq_v+gz$, L the latent heat of condensation, and Q_R and Q_A indicate the radiation and large-scale advection effects, respectively.

The conservation equation for each water species is given by

$$\frac{dq_x}{dt}=\frac{1}{\rho_0}\left[\frac{\partial}{\partial z}\left(\rho_0 V_x q_x\right)\right]-\frac{1}{\rho_0}\left[\frac{\partial}{\partial x}\left(\rho_0\overline{u''q''_x}\right)+\frac{\partial}{\partial y}\left(\rho_0\overline{v''q''_x}\right)+\frac{\partial}{\partial z}\left(\rho_0\overline{w''q''_x}\right)\right]$$
$$+P_x+C_x+Q_{A,x}, \quad (2.12)$$

where the subscript x denotes water vapor (v), cloud water (c), cloud ice (i), rain water (r), snow (s) or graupel (g), $V(\geq 0)$ the mass-weighted fall speed for precipitating particles with $V_v=V_c=V_i=0$, P the net production rate due to the microphysical processes, and C the source of cloud water and cloud ice due to condensation, deposition, evaporation and sublimation with $C_r=C_s=C_g=0$.

b. Predicting the vorticity field

The vorticity equations (2.8)-(2.10) can be rewritten as

$$\rho_0\frac{\partial\xi}{\partial t}=-\left[\frac{\partial}{\partial x}\left(\rho_0 u\xi\right)+\frac{\partial}{\partial y}\left(\rho_0 v\xi\right)+\frac{\partial}{\partial z}\left(\rho_0 w\xi\right)\right]+\rho_0\xi\frac{\partial u}{\partial x}+\rho_0\eta\frac{\partial u}{\partial y}+\rho_0\zeta\frac{\partial u}{\partial z}$$
$$+f\frac{\partial u}{\partial z}+\frac{\partial B}{\partial y}+\frac{\partial F_w}{\partial y}-\frac{\partial F_v}{\partial z}, \quad (2.13)$$

$$\rho_0\frac{\partial\eta}{\partial t}=-\left[\frac{\partial}{\partial x}\left(\rho_0 u\eta\right)+\frac{\partial}{\partial y}\left(\rho_0 v\eta\right)+\frac{\partial}{\partial z}\left(\rho_0 w\eta\right)\right]+\rho_0\eta\frac{\partial v}{\partial y}+\rho_0\xi\frac{\partial v}{\partial x}+\rho_0\zeta\frac{\partial v}{\partial z}$$
$$+f\frac{\partial v}{\partial z}-\frac{\partial B}{\partial x}-\frac{\partial F_w}{\partial x}+\frac{\partial F_u}{\partial z}, \quad (2.14)$$

$$\rho_0 \frac{\partial \zeta}{\partial t} = -\left[\frac{\partial}{\partial x}(\rho_0 u\zeta) + \frac{\partial}{\partial y}(\rho_0 v\zeta) + \frac{\partial}{\partial z}(\rho_0 w\zeta) \right] + \rho_0 \zeta \frac{\partial w}{\partial z} + \rho_0 \xi \frac{\partial w}{\partial x} + \rho_0 \eta \frac{\partial w}{\partial y}$$
$$-f\left(\frac{\partial u}{\partial x} + \frac{\partial v}{\partial y} \right) + \frac{\partial F_v}{\partial x} - \frac{\partial F_u}{\partial y}. \qquad (2.15)$$

In each of (2.13), (2.14) and (2.15), the first term after the brackets represents the stretching effect and the two subsequent terms represent the twisting effect.

From the diagnostic relation (2.7), ζ at an arbitrary height can be obtained through

$$(\rho_0 \zeta)_z = -\int_{z_T}^{z} \left[\frac{\partial(\rho_0 \xi)}{\partial x} + \frac{\partial(\rho_0 \eta)}{\partial y} \right] dz + (\rho_0 \zeta)_{z_T}. \qquad (2.16)$$

Thus, when (2.13) and (2.14) are applied to everywhere, we need to apply (2.15) only at a certain level, $z = z_T$ for example, where the subscript T denotes the upper boundary.

c. Updating the vertical component of velocity

After updating the horizontal components of the vorticity using (2.13) and (2.14), we update the vertical velocity. Operating $\partial/\partial x$ on η and $\partial/\partial y$ on ξ in (2.6), we obtain

$$\frac{\partial^2 w}{\partial x^2} - \frac{\partial^2 u}{\partial x \partial z} = -\frac{\partial}{\partial x}\rho_0 \eta, \qquad (2.17)$$

$$\frac{\partial^2 w}{\partial y^2} - \frac{\partial^2 v}{\partial y \partial z} = \frac{\partial}{\partial y}\rho_0 \xi. \qquad (2.18)$$

With the anelastic continuity equation (2.1), the sum of (2.17) and (2.18) becomes

$$\left(\frac{\partial^2}{\partial x^2} + \frac{\partial^2}{\partial y^2} \right) w + \frac{\partial}{\partial z}\left[\frac{1}{\rho_0} \frac{\partial}{\partial z}(\rho_0 w) \right] = -\rho_0 \frac{\partial \eta}{\partial x} + \rho_0 \frac{\partial \xi}{\partial y}. \qquad (2.19)$$

We can determine w by solving the three-dimensional elliptic equation (2.19) with the upper and lower boundary conditions for w. When these boundaries are horizontal rigid planes, we have

$$w = 0 \quad \text{at the lower and upper boundaries.} \tag{2.20}$$

d. Updating the horizontal components of velocity

To obtain the non-uniform part of the horizontal velocity at the upper boundary, we divide the velocity into the rotational and divergent parts through

$$u = u_\psi + u_\chi \text{ and } v = v_\psi + v_\chi, \tag{2.21}$$

where

$$u_\psi = -\frac{\partial \psi}{\partial y},\ u_\chi = \frac{\partial \chi}{\partial x},\ v_\psi = \frac{\partial \psi}{\partial x},\ v_\chi = \frac{\partial \chi}{\partial y}. \tag{2.22}$$

The streamfunction ψ can be updated solving the two-dimensional elliptic equation

$$\frac{\partial^2 \psi}{\partial x^2} + \frac{\partial^2 \psi}{\partial y^2} = \rho_0 \zeta \tag{2.23}$$

using ζ predicted by (2.15) at the upper boundary. The velocity potential for the divergent part is obtained from the solution of

$$\left(\frac{\partial^2}{\partial x^2} + \frac{\partial^2}{\partial y^2} \right) \chi = -\frac{1}{\rho_0} \frac{\partial}{\partial z} (\rho_0 w) \tag{2.24}$$

using the vertical velocity w determined by (2.19).

We then predict the horizontally uniform part of the horizontal velocity at the upper boundary by

$$\frac{\partial \overline{u}^{xy}}{\partial t} = -\frac{1}{\rho_0} \frac{\partial}{\partial z} \left(\rho_0 \overline{uw}^{xy} \right) + \overline{fv}^{xy} + \overline{F}_u^{xy}, \tag{2.25}$$

$$\frac{\partial \overline{v}^{xy}}{\partial t} = -\frac{1}{\rho_0}\frac{\partial}{\partial z}\left(\rho_0 \overline{vw}^{xy}\right) - \overline{fu}^{xy} + \overline{F}_v^{xy}, \tag{2.26}$$

where $\overline{(\ )}^{xy}$ represents the horizontal average.

To update the horizontal velocity components below the upper boundary, we use (2.6) rewritten as

$$\frac{\partial u}{\partial z} = \frac{\partial w}{\partial x} + \rho_0 \eta, \ \frac{\partial v}{\partial z} = \frac{\partial w}{\partial y} - \rho_0 \xi \ . \tag{2.27}$$

Integrating (2.27) with respect to z downward, we obtain

$$u = \int_{z_T}^{z}\left(\frac{\partial w}{\partial x} + \rho_0 \eta\right)dz + u_T(x,y,t), \ v = \int_{z_T}^{z}\left(\frac{\partial w}{\partial y} - \rho_0 \xi\right)dz + v_T(x,y,t), \tag{2.28}$$

where the subscript T denotes the upper boundary and z_T is assumed to be constant.

3. Discretization of equations

a. Arrangement of variables on the model grid

The main variables and their locations in the vertical and horizontal grids are shown in Figs. 1 and 2, respectively. The model atmosphere is divided into **K** layers identified by integer indices. Interfaces of these layers are identified by half-integer indices (Fig. 1). These indices increase upward. All thermodynamic variables are located at the θ-point. This vertical grid structure, which is similar to the Lorenz grid in quasi-static models, is not the best vertical grid in simulating hydrostatic adjustment in nonhydrostatic models in a Eulerian vertical grid. But it has been chosen in this model to maintain the continuity from its two-dimensional predecessor. A three-dimensional view of the grids is presented in Fig.3.

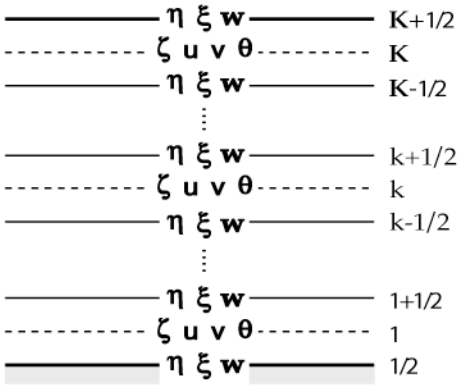

Fig. 1. Vertical grids used in the discretization.

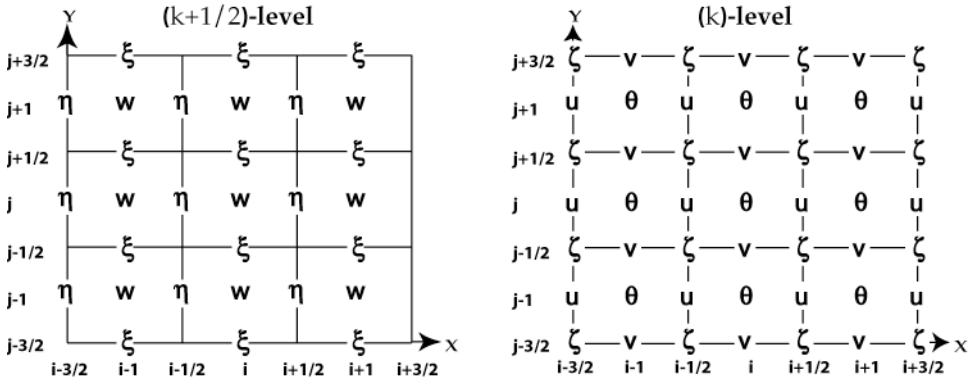

Fig. 2. Horizontal grids used in the discretization.

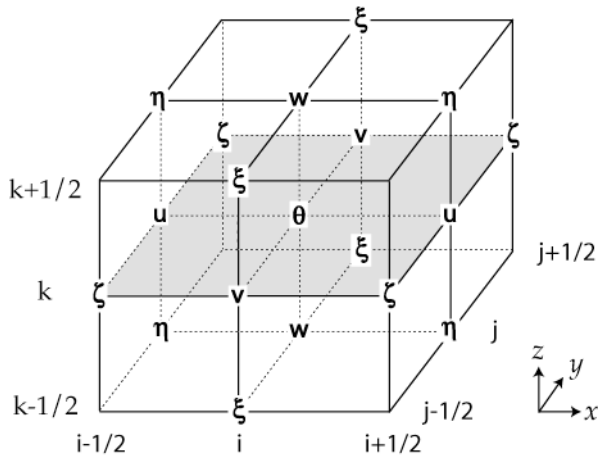

Fig. 3. A three-dimensional view of the model grids.

b. Stretched vertical grid

Following Krueger (1988), a stretched vertical grid is generally used in the model to increase the vertical resolution near the surface. The transformation formula for mapping the physical coordinate, z, onto the map coordinate, z', is as follows:

$$z = \left(c_1 + c_2 z'\right) z' . \tag{3.1}$$

Here $c_1 = 0.172413$ and $c_2 = 5.517 \times 10^{-5}$. The vertical derivative of any variable A is transformed according to

$$\frac{\partial A}{\partial z} = m \frac{\partial A}{\partial z'} \tag{3.2}$$

where m is the map factor given by $m = dz'/dz = 1/\left(c_1 + 2c_2 z'\right)$. On the map coordinate, a constant grid interval, $\delta z'$ (=500 m), is currently used. In the experiments described in section 6, however, a vertically uniform grid is used instead.

c. Advection scheme for scalar variables

The advection scheme for scalar variables used in the model is a generalization of a scheme for the one-dimensional advection equation given by

$$\frac{\partial q}{\partial t} = -U\frac{\partial q}{\partial x}. \tag{3.3}$$

Here q represents an arbitrary scalar and $U(>0)$ is the velocity of a uniform flow in the x-direction. We consider a finite-difference approximation to (3.3) that has the form

$$\frac{\partial q_i}{\partial t} = -\frac{U}{d}\left(\alpha q_{i+1} + \beta q_i + \gamma q_{i-1} + \delta q_{i-2}\right). \tag{3.4}$$

We can show that the scheme has a third-order accuracy if

$$\alpha = \frac{1}{3}, \beta = \frac{1}{2}, \gamma = -1, \delta = \frac{1}{6} \tag{3.5}$$

so that (3.4) can be written as

$$\frac{\partial q_i}{\partial t} = -\frac{U}{6d}\left(2q_{i+1} + 3q_i - 6q_{i-1} + q_{i-2}\right). \tag{3.6}$$

This scheme can be further rewritten as

$$\begin{cases} \text{advective form}: & \dfrac{\partial q_i}{\partial t} = -\dfrac{U}{6d}\left[2\left(q_{i+1} - q_i\right) + 5\left(q_i - q_{i-1}\right) - \left(q_{i-1} - q_{i-2}\right)\right], \\ \text{flux form}: & \dfrac{\partial q_i}{\partial t} = -\dfrac{U}{6d}\left[\left(2q_{i+1} + 5q_i - q_{i-1}\right) - \left(2q_i + 5q_{i-1} - q_{i-2}\right)\right]. \end{cases} \tag{3.7}$$

A generalization of the flux form (3.7) to include a second-order scheme is given by

$$\frac{\partial q_i}{\partial t} = -\frac{U}{2d}\left\{\left[\left(q_{i+1} + q_i\right) - \frac{\alpha}{3}\left(q_{i+1} - 2q_i + q_{i-1}\right)\right] - \left[\left(q_i + q_{i-1}\right) - \frac{\alpha}{3}\left(q_i - 2q_{i-1} + q_{i-2}\right)\right]\right\}, \tag{3.8}$$

where α is a parameter. The scheme (3.8) becomes a third-order scheme when $\alpha = 1$ and the centered second-order scheme when $\alpha = 0$.

Considering a flow in the positive directions of x and y, we further generalize (3.8), as Takacs (1985) did, to the case of two-dimensional nondivergent flow as

$$\frac{\partial q_{i,j}}{\partial t}$$
$$= -\frac{1}{2d}\Big\langle \Big\{ u_{i+1/2,j}\left(q_{i+1,j}+q_{i,j}\right) - \frac{\alpha}{3}\Big[u_{i+1/2,j}\left(q_{i+1,j}-q_{i,j}\right) - \sqrt{u_{i+1/2,j}}\sqrt{u_{i-1/2,j}}\left(q_{i,j}-q_{i-1,j}\right)\Big]\Big\}$$
$$-\Big\{ u_{i-1/2,j}\left(q_{i,j}+q_{i-1,j}\right) - \frac{\alpha}{3}\Big[u_{i-1/2,j}\left(q_{i,j}-q_{i-1,j}\right) - \sqrt{u_{i-1/2,j}}\sqrt{u_{i-3/2,j}}\left(q_{i-1,j}-q_{i-2,j}\right)\Big]\Big\}\Big\rangle$$
$$-\frac{1}{2d}\Big\langle \Big\{ v_{i,j+1/2}\left(q_{i,j+1}+q_{i,j}\right) - \frac{\alpha}{3}\Big[v_{i,j+1/2}\left(q_{i,j+1}-q_{i,j}\right) - \sqrt{v_{i,j+1/2}}\sqrt{v_{i,j-1/2}}\left(q_{i,j}-q_{i,j-1}\right)\Big]\Big\}$$
$$-\Big\{ v_{i,j-1/2}\left(q_{i,j}+q_{i,j-1}\right) - \frac{\alpha}{3}\Big[v_{i,j-1/2}\left(q_{i,j}-q_{i,j-1}\right) - \sqrt{v_{i,j-1/2}}\sqrt{v_{i,j-3/2}}\left(q_{i,j-1}-q_{i,j-2}\right)\Big]\Big\}\Big\rangle . \tag{3.9}$$

To show that the solutions of this scheme are quadratically bounded, we multiply (3.9) by $q_{i,j}$ to obtain

$$\frac{1}{2}\frac{\partial q_{i,j}^2}{\partial t} = -\frac{1}{2d}\Big\langle \Big\{ u_{i+1/2,j}q_{i,j}q_{i+1,j} - u_{i-1/2,j}q_{i,j}q_{i-1,j} + \left(u_{i+1/2,j}-u_{i-1/2,j}\right)q_{i,j}^2\Big\}$$
$$-\frac{1}{3}\alpha\Big[u_{i+1/2}\left(q_{i+1}-q_i\right)q_i - \sqrt{u_{i+1/2}}\sqrt{u_{i-1/2}}\left(q_i-q_{i-1}\right)q_i$$
$$-u_{i-1/2,j}\left(q_{i,j}-q_{i-1,j}\right)q_{i,j} + \sqrt{u_{i-1/2,j}}\sqrt{u_{i-3/2,j}}\left(q_{i-1,j}-q_{i-2,j}\right)q_{i,j}\Big]\Big\rangle . \tag{3.10}$$

Here only the advection terms due to the x-component of the flow are written. The last term in the braces on the first line is canceled by the corresponding term in the y direction due to the nondivergence of the flow. Also, the first and second terms in the braces vanish when their sum is taken over all grid points in the x-direction in a cyclic domain. Then the sum of (3.10) becomes

$$\frac{1}{2}\frac{\partial}{\partial t}\sum_i q_{i,j}^2 = \frac{\alpha}{6d}\sum_i\Big\{ -u_{i+1/2,j}\left(q_{i+1,j}-q_{i,j}\right)^2 + \sqrt{u_{i+1/2,j}}\sqrt{u_{i-1/2,j}}\left(q_{i,j}-q_{i-1,j}\right)\left(q_{i+1,j}-q_{i,j}\right)\Big\}$$
$$= -\frac{\alpha}{12d}\sum_i\Big[\sqrt{u_{i+1/2,j}}\left(q_{i+1,j}-q_{i,j}\right) - \sqrt{u_{i-1/2,j}}\left(q_{i,j}-q_{i-1,j}\right)\Big]^2 . \tag{3.11}$$

Thus, when the flow is nondivergent, the sum of $q_{i,j}^2$ is bounded and stability is guaranteed as long as time is continuous.

The scheme is further generalized to an arbitrary three-dimensional advective flow as below,

$$\frac{\partial q_{i,j,k}}{\partial t} = -\frac{1}{2}\left[\frac{1}{dx}\left(F^{q}_{i+1/2,j,k} - F^{q}_{i-1/2,j,k}\right) + \frac{1}{dy}\left(F^{q}_{i,j+1/2,k} - F^{q}_{i,j-1/2,k}\right) + \frac{m_k}{\rho_{0,k}dz'}\left(F^{q}_{i,j,k+1/2} - F^{q}_{i,j,k-1/2}\right)\right], \tag{3.12}$$

where m is the map factor,

$$\begin{aligned} F^{q}_{i+1/2,j,k} \equiv \Big\{ & u_{i+1/2,j,k}\left(q_{i+1,j,k} + q_{i,j,k}\right) \\ & -\frac{\alpha}{3}\Big[u^{+}_{i+1/2}\left(q_{i+1,j,k} - q_{i,j,k}\right) - \sqrt{u^{+}_{i+1/2}}\sqrt{u^{+}_{i-1/2}}\left(q_{i,j,k} - q_{i-1,j,k}\right) \\ & -u^{-}_{i+1/2}\left(q_{i+1,j,k} - q_{i,j,k}\right) - \sqrt{\left|u^{-}_{i+1/2}\right|}\sqrt{\left|u^{-}_{i+3/2}\right|}\left(q_{i+2,j,k} - q_{i+1,j,k}\right)\Big]\Big\}, \end{aligned} \tag{3.13}$$

$$\begin{aligned} F^{q}_{i,j+1/2,k} \equiv \Big\{ & v_{i,j+1/2,k}\left(q_{i,j+1,k} + q_{i,j,k}\right) \\ & -\frac{\alpha}{3}\Big[v^{+}_{j+1/2}\left(q_{i,j+1,k} - q_{i,j,k}\right) - \sqrt{v^{+}_{j+1/2}}\sqrt{v^{+}_{j-1/2}}\left(q_{i,j,k} - q_{i,j-1,k}\right) \\ & -v^{-}_{j+1/2}\left(q_{i,j+1,k} - q_{i,j,k}\right) - \sqrt{\left|v^{-}_{j+1/2}\right|}\sqrt{\left|v^{-}_{j+3/2}\right|}\left(q_{i,j+2,k} - q_{i,j+1,k}\right)\Big]\Big\}, \end{aligned} \tag{3.14}$$

$$\begin{aligned} F^{q}_{i,j,k+1/2} \equiv \Big\{ & \rho_{0,k+1/2}w_{i,j,k+1/2}\left(q_{i,j,k+1} + q_{i,j,k}\right) \\ & -\frac{\alpha}{3}\Big[w^{+}_{k+1/2}\left(q_{i,j,k+1} - q_{i,j,k}\right) - \sqrt{w^{+}_{k+1/2}}\sqrt{w^{+}_{k-1/2}}\left(q_{i,j,k} - q_{i,j,k-1}\right) \\ & -w^{-}_{k+1/2}\left(q_{i,j,k+1} - q_{i,j,k}\right) - \sqrt{\left|w^{-}_{k+1/2}\right|}\sqrt{\left|w^{-}_{k+3/2}\right|}\left(q_{i,j,k+2} - q_{i,j,k+1}\right)\Big]\Big\}, \end{aligned} \tag{3.15}$$

and

$$\begin{cases} u^{\pm}_{i+1/2} = \dfrac{u_{i+1/2,j,k} \pm \left|u_{i+1/2,j,k}\right|}{2}, \\ v^{\pm}_{j+1/2} = \dfrac{v_{i,j+1/2,k} \pm \left|v_{i,j+1/2,k}\right|}{2}, \quad \text{and} \\ w^{\pm}_{k+1/2} = \rho_{0,k+1/2}\dfrac{w_{i,j,k+1/2} \pm \left|w_{i,j,k+1/2}\right|}{2}. \end{cases} \tag{3.16}$$

d. Discretization of the vorticity equation

1) Continuous enstrophy equation

We first derive the enstrophy equation in its continuous form through operating $\xi\times$(2.13), $\eta\times$(2.14), and $\zeta\times$(2.15) (without the Coriolis force, buoyancy and friction terms for simplicity) to yield

$$\rho_0\frac{\partial}{\partial t}\left(\frac{\xi^2}{2}\right)=-\left[\frac{\partial}{\partial x}\left(\rho_0 u\frac{\xi^2}{2}\right)+\frac{\partial}{\partial y}\left(\rho_0 v\frac{\xi^2}{2}\right)+\frac{\partial}{\partial z}\left(\rho_0 w\frac{\xi^2}{2}\right)\right] +\rho_0\xi^2\frac{\partial u}{\partial x}+\rho_0\xi\eta\frac{\partial u}{\partial y}+\rho_0\xi\zeta\frac{\partial u}{\partial z}, \tag{3.17}$$

$$\rho_0\frac{\partial}{\partial t}\left(\frac{\eta^2}{2}\right)=-\left[\frac{\partial}{\partial x}\left(\rho_0 u\frac{\eta^2}{2}\right)+\frac{\partial}{\partial y}\left(\rho_0 v\frac{\eta^2}{2}\right)+\frac{\partial}{\partial z}\left(\rho_0 w\frac{\eta^2}{2}\right)\right] +\rho_0\eta^2\frac{\partial v}{\partial y}+\rho_0\eta\xi\frac{\partial v}{\partial x}+\rho_0\eta\zeta\frac{\partial v}{\partial z}, \tag{3.18}$$

$$\rho_0\frac{\partial}{\partial t}\left(\frac{\zeta^2}{2}\right)=-\left[\frac{\partial}{\partial x}\left(\rho_0 u\frac{\zeta^2}{2}\right)+\frac{\partial}{\partial y}\left(\rho_0 v\frac{\zeta^2}{2}\right)+\frac{\partial}{\partial z}\left(\rho_0 w\frac{\zeta^2}{2}\right)\right] +\rho_0\zeta^2\frac{\partial w}{\partial z}+\rho_0\zeta\xi\frac{\partial w}{\partial x}+\rho_0\zeta\eta\frac{\partial w}{\partial y}. \tag{3.19}$$

Taking the sum of these equations and averaging the results over the entire volume, we can obtain the mass weighted mean enstrophy equation as

$$\frac{\partial}{\partial t}\overline{\rho_0\left(\frac{\xi^2+\eta^2+\zeta^2}{2}\right)}=\overline{\rho_0\left(\xi^2\frac{\partial u}{\partial x}+\eta^2\frac{\partial v}{\partial y}+\zeta^2\frac{\partial w}{\partial z}\right)} +\overline{\rho_0\xi\eta\left(\frac{\partial v}{\partial x}+\frac{\partial u}{\partial y}\right)}+\overline{\rho_0\zeta\eta\left(\frac{\partial w}{\partial y}+\frac{\partial v}{\partial z}\right)}+\overline{\rho_0\zeta\xi\left(\frac{\partial w}{\partial x}+\frac{\partial u}{\partial z}\right)}, \tag{3.20}$$

where an over bar denotes the volume average. Without the stretching and deformation effects, the mass-weighted mean enstrophy is conserved. Keeping this in mind, we descretize the individual terms in the vorticity equations as below.

2) Discretization of the flux convergence terms

As in (3.12), the first term in the right-hand-side of (2.13) can be written as,

$$-\left[\frac{\partial}{\partial x}\left(\rho_0 u\xi\right)\right]_{i,j+1/2,k+1/2} = -\frac{1}{2dx}\left(F^{\xi}_{i+1/2,j+1/2,k+1/2} - F^{\xi}_{i-1/2,j+1/2,k+1/2}\right), \tag{3.21}$$

where

$$\begin{aligned} F^{\xi}_{i+1/2,j+1/2,k+1/2} \equiv \Big\{ & U_{i+1/2,j+1/2,k+1/2}\left(\xi_{i+1,j+1/2,k+1/2} + \xi_{i,j+1/2,k+1/2}\right) \\ & -\frac{\alpha}{3}\Big[U^{+}_{i+1/2,j+1/2,k+1/2}\left(\xi_{i+1,j+1/2,k+1/2} - \xi_{i,j+1/2,k+1/2}\right) \\ & -\sqrt{U^{+}_{i+1/2,j+1/2,k+1/2}}\sqrt{U^{+}_{i-1/2,j+1/2,k+1/2}}\left(\xi_{i,j+1/2,k+1/2} - \xi_{i-1,j+1/2,k+1/2}\right) \\ & -U^{-}_{i+1/2,j+1/2,k+1/2}\left(\xi_{i+1,j+1/2,k+1/2} - \xi_{i,j+1/2,k+1/2}\right) \\ & -\sqrt{\left|U^{-}_{i+1/2,j+1/2,k+1/2}\right|}\sqrt{\left|U^{-}_{i+3/2,j+1/2,k+1/2}\right|}\left(\xi_{i+2,j+1/2,k+1/2} - \xi_{i+1,j+1/2,k+1/2}\right)\Big]\Big\}, \end{aligned} \tag{3.22}$$

$$U_{i+1/2,j+1/2,k+1/2} \equiv \frac{1}{4}\left\{\left[\rho_{0,k+1}\left(u_{i+1/2,j,k+1} + u_{i+1/2,j+1,k+1}\right) + \rho_{0,k}\left(u_{i+1/2,j,k} + u_{i+1/2,j+1,k}\right)\right]\right\}, \tag{3.23}$$

$$U^{\pm}_{i+1/2,j+1/2,k+1/2} = \left(\frac{U_{i+1/2,j+1/2,k+1/2} \pm \left|U_{i+1/2,j+1/2,k+1/2}\right|}{2}\right). \tag{3.24}$$

Here U is a linear combination of u at neighboring grid points following the way used in the second-order enstrophy conserving Jacobian J6 defined by Arakawa and Lamb (1977). Thus, even when $\alpha = 1$, this scheme is *partially* third order for non-uniform flow. Similar discretizations are used for the second and third terms in (2.13) and the first three terms in (2.14) and (2.15).

3) Discretization of the stretching terms

The stretching terms in (2.13)-(2.15) are discretized as follows:

$$\left[\rho_0\xi\frac{\partial u}{\partial x}\right]_{i,j+1/2,k+1/2} = \frac{1}{8dx}\left\{\left[\rho_{0,k+1}\left(u_{i+1/2,j+1,k+1} - u_{i-1/2,j+1,k+1}\right) + \rho_{0,k}\left(u_{i+1/2,j+1,k} - u_{i-1/2,j+1,k}\right)\right]\right.$$

$$\times\left(\xi_{i,j+1/2,k+1/2}+\xi_{i,j+3/2,k+1/2}\right)+\left[\rho_{0,k+1}\left(u_{i+1/2,j,k+1}-u_{i-1/2,j,k+1}\right)+\rho_{0,k}\left(u_{i+1/2,j,k}-u_{i-1/2,j,k}\right)\right]$$
$$\times\left(\xi_{i,j-1/2,k+1/2}+\xi_{i,j+1/2,k+1/2}\right)\Big\}, \tag{3.25}$$

$$\left[\rho_0\eta\frac{\partial v}{\partial y}\right]_{i+1/2,j,k+1/2}=\frac{1}{8dy}\Big\{\left[\rho_{0,k+1}\left(v_{i,j+1/2,k+1}-v_{i,j-1/2,k+1}\right)+\rho_{0,k}\left(v_{i,j+1/2,k}-v_{i,j-1/2,k}\right)\right]$$
$$\times\left(\eta_{i-1/2,j,k+1/2}+\eta_{i+1/2,j,k+1/2}\right)+\left[\rho_{0,k+1}\left(v_{i+1,j+1/2,k+1}-v_{i+1,j-1/2,k+1}\right)+\rho_{0,k}\left(v_{i+1,j+1/2,k}-v_{i+1,j-1/2,k}\right)\right]$$
$$\times\left(\eta_{i+1/2,j,k+1/2}+\eta_{i+3/2,j,k+1/2}\right)\Big\}, \tag{3.26}$$

and

$$\left[\rho_0\varsigma\frac{\partial w}{\partial z}\right]_{i+1/2,j+1/2,k}$$
$$=\frac{\rho_{0,k}}{8dz}\Big\{\left[\left(w_{i,j,k+1/2}-w_{i,j,k-1/2}\right)+\left(w_{i,j+1,k+1/2}-w_{i,j+1,k-1/2}\right)\right]\left(\zeta_{i-1/2,j+1/2,k}+\zeta_{i+1/2,j+1/2,k}\right)$$
$$+\left[\left(w_{i+1,j,k+1/2}-w_{i+1,j,k-1/2}\right)+\left(w_{i+1,j+1,k+1/2}-w_{i+1,j+1,k-1/2}\right)\right]\left(\zeta_{i+1/2,j+1/2,k}+\zeta_{i+3/2,j+1/2,k}\right)\Big\}. \tag{3.27}$$

4) Discretization of the twisting terms

The twisting terms in (2.13)-(2.15) can be rewritten as

$$\left(\rho_0\eta\frac{\partial u}{\partial y}\right)+\left(\rho_0\zeta\frac{\partial u}{\partial z}\right)=\frac{\rho_0}{2}\left(\eta R^{\zeta}+\zeta R^{\eta}\right), \tag{3.28}$$

$$\left(\rho_0\xi\frac{\partial v}{\partial x}\right)+\left(\rho_0\zeta\frac{\partial v}{\partial z}\right)=\frac{\rho_0}{2}\left(\xi R^{\zeta}+\zeta R^{\xi}\right), \tag{3.29}$$

$$\left(\rho_0\xi\frac{\partial w}{\partial x}\right)+\left(\rho_0\eta\frac{\partial w}{\partial y}\right)=\frac{\rho_0}{2}\left(\xi R^{\eta}+\eta R^{\xi}\right), \tag{3.30}$$

where

$$R^{\xi}\equiv\left(\frac{\partial w}{\partial y}+\frac{\partial v}{\partial z}\right),\quad R^{\eta}\equiv\left(\frac{\partial w}{\partial x}+\frac{\partial u}{\partial z}\right),\quad R^{\zeta}\equiv\left(\frac{\partial v}{\partial x}+\frac{\partial u}{\partial y}\right). \tag{3.31}$$

These quantities are discretized as

$$\begin{cases} R^{\xi}_{i,j+1/2,k+1/2} = \left(\dfrac{w_{i,j+1,k+1/2} - w_{i,j,k+1/2}}{dy} + \dfrac{v_{i,j+1/2,k+1} - v_{i,j+1/2,k}}{dz} \right) \\ R^{\eta}_{i+1/2,j,k+1/2} = \left(\dfrac{w_{i+1,j,k+1/2} - w_{i,j,k+1/2}}{dx} + \dfrac{u_{i+1/2,j,k+1} - u_{i+1/2,j,k}}{dz} \right) \\ R^{\zeta}_{i+1/2,j+1/2,k+1} = \left(\dfrac{v_{i+1,j+1/2,k+1} - v_{i,j+1/2,k+1}}{dx} + \dfrac{u_{i+1/2,j+1,k+1} - u_{i+1/2,j,k+1}}{dy} \right) \end{cases} . \qquad (3.32)$$

The variables R^{ξ}, R^{η}, and R^{ζ} are located at the ξ-, η-, and ζ-points, respectively. Then, the right-hand-side of (3.28) is discretized as

$$\begin{aligned} &\left[\frac{\rho_0}{2} \left(\eta R^{\zeta} + \zeta R^{\eta} \right) \right]_{i,j+1/2,k+1/2} \\ &= \frac{\rho_{0,k+1/2}}{16} \left\{ \left(\eta_{i+1/2,j+1,k+1/2} + \eta_{i+1/2,j,k+1/2} \right) \left(\frac{\rho_{0,k}}{\rho_{0,k+1/2}} R^{\zeta}_{i+1/2,j+1/2,k} + \frac{\rho_{0,k+1}}{\rho_{0,k+1/2}} R^{\zeta}_{i+1/2,j+1/2,k+1} \right) \right. \\ &\qquad \left. + \left(\eta_{i-1/2,j+1,k+1/2} + \eta_{i-1/2,j,k+1/2} \right) \left(\frac{\rho_{0,k}}{\rho_{0,k+1/2}} R^{\zeta}_{i-1/2,j+1/2,k} + \frac{\rho_{0,k+1}}{\rho_{0,k+1/2}} R^{\zeta}_{i-1/2,j+1/2,k+1} \right) \right\} \\ &+ \frac{1}{16} \left\{ \left(\rho_{0,k} \zeta_{i+1/2,j+1/2,k} + \rho_{0,k+1} \zeta_{i+1/2,j+1/2,k+1} \right) \left(R^{\eta}_{i+1/2,j+1,k+1/2} + R^{\eta}_{i+1/2,j,k+1/2} \right) \right. \\ &\left. + \left(\rho_{0,k} \zeta_{i-1/2,j+1/2,k} + \rho_{0,k+1} \zeta_{i-1/2,j+1/2,k+1} \right) \left(R^{\eta}_{i-1/2,j+1,k+1/2} + R^{\eta}_{i-1/2,j,k+1/2} \right) \right\} . \end{aligned} \qquad (3.33)$$

Similar discretizations are used for the right-hand-side of (3.29) and (3.30).

e. Solving the 3-D elliptic equation

Consider the 3-D elliptic equation (2.19) with the boundary condition $w = 0$ at the lower and upper-boundaries:

$$\frac{\partial^2}{\partial x^2} \left(\rho_0 w \right) + \frac{\partial^2}{\partial y^2} \left(\rho_0 w \right) + \rho_o \frac{\partial}{\partial z} \left[\frac{1}{\rho_0} \frac{\partial}{\partial z} \left(\rho_0 w \right) \right] = -\rho_0^2 \frac{\partial \eta}{\partial x} + \rho_0^2 \frac{\partial \xi}{\partial y} . \qquad (3.34)$$

The second-order centered finite difference form of (3.34) may be written as

$$\frac{1}{\Delta x^2}\left[(\rho_0 w)_{i-1,j,k+1/2} - 2(\rho_0 w)_{i,j,k+1/2} + (\rho_0 w)_{i+1,j,k+1/2}\right]$$
$$+\frac{1}{\Delta y^2}\left[(\rho_0 w)_{i,j-1,k+1/2} - 2(\rho_0 w)_{i,j,k+1/2} + (\rho_0 w)_{i,j+1,k+1/2}\right]$$
$$+A_{k+1/2}(\rho_0 w)_{i,j,k-1/2} + B_{k+1/2}(\rho_0 w)_{i,j,k+1/2} + C_{k+1/2}(\rho_0 w)_{i,j,k+3/2} = F_{i,j,k+1/2}, \qquad (3.35)$$

where,

$$F_{i,j,k+1/2} = -\rho_{0,k+1/2}\left\{\frac{\left[(\rho_0\eta)_{i,j,k+1/2} - (\rho_0\eta)_{i-1,j,k+1/2}\right]}{\Delta x} - \frac{\left[(\rho_0\xi)_{i,j,k+1/2} - (\rho_0\xi)_{i,j-1,k+1/2}\right]}{\Delta y}\right\}, \qquad (3.36)$$

$$\begin{cases} A_{k+1/2} = \left(\dfrac{m_k}{\rho_{0,k}}\right)\dfrac{m_{k+1/2}\rho_{0,k+1/2}}{\Delta z'^2}, \\ B_{k+1/2} = -\dfrac{m_{k+1/2}\rho_{0,k+1/2}}{\Delta z'^2}\left(\dfrac{m_k}{\rho_{0,k}} + \dfrac{m_{k+1}}{\rho_{0,k+1}}\right) = -\left(A_{k+1/2} + C_{k+1/2}\right), \\ C_{k+1/2} = \left(\dfrac{m_{k+1}}{\rho_{0,k+1}}\right)\dfrac{m_{k+1/2}\rho_{0,k+1/2}}{\Delta z'^2}, \end{cases} \qquad (3.37)$$

and m is a map factor.

For the level k=1+1/2, next to the lower boundary, (3.35) is replaced by

$$\frac{1}{\Delta x^2}\left[(\rho_0 w)_{i-1,j,1+1/2} - 2(\rho_0 w)_{i,j,1+1/2} + (\rho_0 w)_{i+1,j,1+1/2}\right]$$
$$+\frac{1}{\Delta y^2}\left[(\rho_0 w)_{i,j-1,1+1/2} - 2(\rho_0 w)_{i,j,1+1/2} + (\rho_0 w)_{i,j+1,1+1/2}\right]$$
$$+B_{1+1/2}(\rho_0 w)_{i,j,1+1/2} + C_{1+1/2}(\rho_0 w)_{i,j,2+1/2} = F_{i,j,1+1/2}, \qquad (3.35a)$$

where

$$F_{i,j,1+1/2} = -\rho_{0,1+1/2}\left\{\frac{\left[(\rho_0\eta)_{i,j,1+1/2} - (\rho_0\eta)_{i-1,j,1+1/2}\right]}{\Delta x} - \frac{\left[(\rho_0\xi)_{i,j,1+1/2} - (\rho_0\xi)_{i,j-1,1+1/2}\right]}{\Delta y}\right\}$$
$$-\left(\frac{m_1}{\rho_{0,1}}\right)\frac{m_{1+1/2}\rho_{0,1+1/2}}{\Delta z'^2}(\rho_0 w)_{i,j,1/2}, \qquad (3.36a)$$

$$\begin{cases} B_{1+1/2} = -\dfrac{m_{1+1/2}\rho_{0,1+1/2}}{\Delta z'^2}\left(\dfrac{m_1}{\rho_{0,1}} + \dfrac{m_2}{\rho_{0,2}}\right), \\ C_{1+1/2} = \left(\dfrac{m_2}{\rho_{0,2}}\right)\dfrac{m_{1+1/2}\rho_{0,1+1/2}}{\Delta z'^2}. \end{cases} \tag{3.37a}$$

For the level k=**K**-1/2, next to the upper boundary, (3.35) is replaced by

$$\begin{aligned} &\frac{1}{\Delta x^2}\left[(\rho_0 w)_{i-1,j,\mathbf{K}-1/2} - 2(\rho_0 w)_{i,j,\mathbf{K}-1/2} + (\rho_0 w)_{i+1,j,\mathbf{K}-1/2}\right] \\ &+\frac{1}{\Delta y^2}\left[(\rho_0 w)_{i,j-1,\mathbf{K}-1/2} - 2(\rho_0 w)_{i,j,\mathbf{K}-1/2} + (\rho_0 w)_{i,j+1,\mathbf{K}-1/2}\right] \\ &+A_{\mathbf{K}-1/2}(\rho_0 w)_{i,j,\mathbf{K}-3/2} + B_{\mathbf{K}-1/2}(\rho_0 w)_{i,j,\mathbf{K}-1/2} = F_{i,j,\mathbf{K}-1/2}, \end{aligned} \tag{3.35b}$$

where

$$\begin{aligned} F_{i,j,\mathbf{K}-1/2} = -\rho_{0,\mathbf{K}-1/2}&\left\{\frac{\left[(\rho_0\eta)_{i,j,\mathbf{K}-1/2} - (\rho_0\eta)_{i-1,j,\mathbf{K}-1/2}\right]}{\Delta x} - \frac{\left[(\rho_0\eta)_{i,j,\mathbf{K}-1/2} - (\rho_0\eta)_{i,j-1,\mathbf{K}-1/2}\right]}{\Delta y}\right\} \\ &-\left(\frac{m_{\mathbf{K}}}{\rho_{0,\mathbf{K}}}\right)\frac{m_{\mathbf{K}-1/2}\rho_{0,\mathbf{K}-1/2}}{\Delta z'^2}(\rho_0 w)_{i,j,\mathbf{K}+1/2}, \end{aligned} \tag{3.36b}$$

$$\begin{cases} A_{\mathbf{K}-1/2} = \left(\dfrac{m_{\mathbf{K}-1}}{\rho_{0,\mathbf{K}-1}}\right)\dfrac{m_{\mathbf{K}-1/2}\rho_{0,\mathbf{K}-1/2}}{\Delta z'^2}, \\ B_{\mathbf{K}-1/2} = -\dfrac{m_{\mathbf{K}-1/2}\rho_{0,\mathbf{K}-1/2}}{\Delta z'^2}\left(\dfrac{m_{\mathbf{K}-1}}{\rho_{0,\mathbf{K}-1}} + \dfrac{m_{\mathbf{K}}}{\rho_{0,\mathbf{K}}}\right). \end{cases} \tag{3.37b}$$

This tri-diagonal linear system is solved using the subroutine named POIS3D in the subroutine package FISHPAK of UCAR for solving separable elliptic partial differential equations.

f. Updating horizontal velocities at the upper boundary

The second-order centered finite difference form of (2.23) is given by

$$a_m \psi_{i-1/2,j+1/2} + b_m \psi_{i+1/2,j+1/2} + c_m \psi_{i+3/2,j+1/2} + a_n \psi_{i+1/2,j-1/2} + b_n \psi_{i+1/2,j+1/2} + c_n \psi_{i+1/2,j+3/2} = F_{i+1/2,j+1/2}, \tag{3.38}$$

where

$$F_{i+1/2,j+1/2} = \zeta_{i+1/2,j+1/2,K}, \tag{3.39}$$

$$\begin{cases} a_m = \dfrac{1}{\Delta x^2}, \quad b_m = -\dfrac{2}{\Delta x^2} = -(a_m + c_m), \quad c_m = \dfrac{1}{\Delta x^2}, \quad \text{and} \\ a_n = \dfrac{1}{\Delta y^2}, \quad b_n = -(a_n + c_n), \quad c_n = \dfrac{1}{\Delta y^2}. \end{cases} \tag{3.40}$$

Next, the second-order centered finite difference form of (2.25) is

$$a_m \chi_{i-1,j} + b_m \chi_{i,j} + c_m \chi_{i+1,j} + a_n \chi_{i,j-1} + b_n \chi_{i,j} + c_n \chi_{i,j+1} = F_{i,j}, \tag{3.41}$$

where

$$F_{i,j} = \frac{1}{\rho_{0,K}} \frac{m_K}{dz'} \left(\rho_{0,K-1/2} w_{i,j,K-1/2} \right), \tag{3.42}$$

$$\begin{cases} a_m = \dfrac{1}{\Delta x^2}, \quad b_m = -\dfrac{2}{\Delta x^2} = -(a_m + c_m), \quad c_m = \dfrac{1}{\Delta x^2}, \quad \text{and} \\ a_n = \dfrac{1}{\Delta y^2}, \quad b_n = -(a_n + c_n), \quad c_n = \dfrac{1}{\Delta y^2}. \end{cases} \tag{3.43}$$

These equation systems are solved with the subroutine named HWSCRT in the subroutine package FISHPAK of UCAR for solving separable elliptic partial equations.

For the model's top layer (k=**K**), the streamfunction ψ and velocity potential χ are defined at ζ-point and θ-point (see Figs. 1 and 2), respectively. From the updated ψ and χ, we obtain

$$\hat{u}_{i+1/2,j,K} = -\left(\frac{\psi_{i+1/2,j+1/2} - \psi_{i+1/2,j-1/2}}{dy} \right) + \left(\frac{\chi_{i+1,j} - \chi_{i,j}}{dx} \right), \tag{3.44}$$

$$\hat{v}_{i,j+1/2,K} = \left(\frac{\psi_{i+1/2,j+1/2} - \psi_{i-1/2,j+1/2}}{dx} \right) + \left(\frac{\chi_{i,j+1} - \chi_{i,j}}{dy} \right). \tag{3.45}$$

The horizontally uniform parts of u and v at the upper boundary are predicted from

$$\rho_0 \frac{\partial \overline{u}^{xy}}{\partial t} = -\frac{\partial}{\partial z}\left(\rho_0 \overline{uw}^{xy}\right) + \rho_0 \overline{fv}^{xy} + \frac{\partial}{\partial z}\left[\rho_0 \overline{K^M R^\eta}^{xy}\right], \tag{3.46}$$

$$\rho_0 \frac{\partial \overline{v}^{xy}}{\partial t} = -\frac{\partial}{\partial z}\left(\rho_0 \overline{vw}^{xy}\right) - \rho_0 \overline{fu}^{xy} + \frac{\partial}{\partial z}\left[\rho_0 \overline{K^M R^\xi}^{xy}\right], \tag{3.47}$$

where $\overline{(\ )}^{xy}$ represents the horizontal average. The finite-difference form of (3.46) is given by

$$\begin{aligned}
&\rho_{0,K} \frac{\partial \overline{u}_K^{xy}}{\partial t} \\
&= -\frac{m_K}{4dz'} \frac{1}{\sum_{i,j}} \Big[\sum_{i,j} \left(\rho_{0,K} u_{i+1/2,j,K} + \rho_{0,K+1} u_{i+1/2,j,K+1}\right)\left(w_{i,j,K+1/2} + w_{i+1,j,K+1/2}\right) \\
&\qquad - \sum_{i,j} \left(\rho_{0,K-1} u_{i+1/2,j,K-1} + \rho_{0,K} u_{i+1/2,j,K}\right)\left(w_{i,j,K-1/2} + w_{i+1,j,K-1/2}\right) \\
&\qquad - \sum_{i,j} \rho_{0,K+1/2} \left(K^M_{i,j,K} + K^M_{i+1,j,K} + K^M_{i,j,K+1} + K^M_{i+1,j,K+1}\right) R^\eta_{i+1/2,j,K+1/2} \\
&\qquad + \sum_{i,j} \rho_{0,K-1/2} \left(K^M_{i,j,K-1} + K^M_{i+1,j,K-1} + K^M_{i,j,K} + K^M_{i+1,j,K}\right) R^\eta_{i+1/2,j,K-1/2} \Big] \\
&\quad + \frac{1}{\sum_{i,j}} \Big[\sum_{i,j} \rho_{0,K} (fv)_{i,j+1/2,K} \Big],
\end{aligned} \tag{3.48}$$

where K^M is the eddy viscosity coefficient defined in (4.5). A similar finite-difference form is used for (3.47).

4. Physical parameterizations

Except for the turbulence parameterization, we use a physics package of the UCLA/CSU/University of Utah two-dimensional cloud model, which has been applied to a variety of cloud regimes including stratocumulus, altocumulus, cumulo-nimbus and cirrus clouds (see, for example, Krueger 2000).

a. Microphysics parameterization

Microphysical processes are parameterized with a bulk method essentially following Lord *et al.* (1984) and Lin *et al.* (1983). Major modifications have been made by Krueger *et al.* (1995) on the growth of cloud ice by the Bergeron process, the conversion of cloud ice to snow, and the characteristics of graupel. Figure 4 shows the structure of the microphysical parameterization.

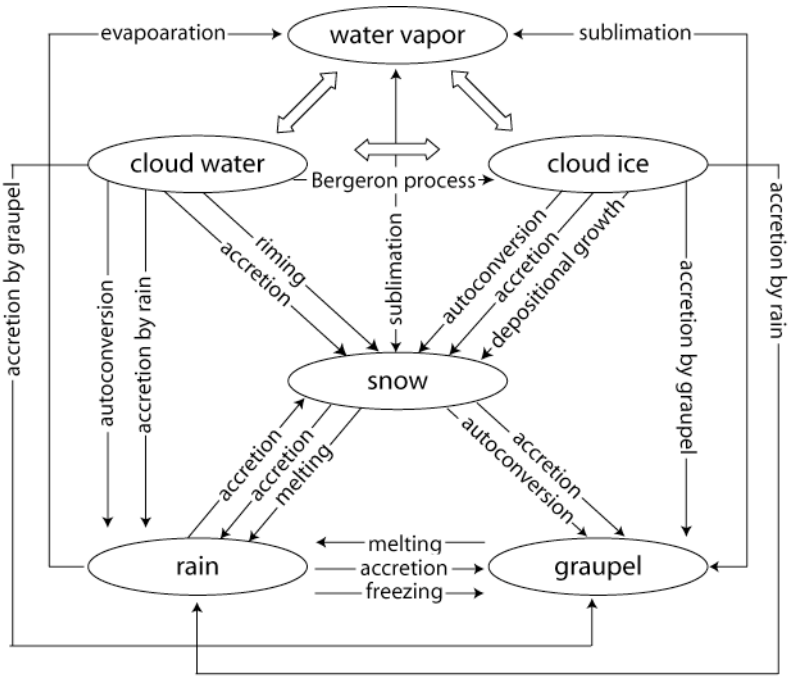

Fig. 4. Microphysical processes parameterized in the model. The broad arrows represent saturation adjustment processes.

b. Radiative transfer parameterization

The radiative transfer scheme used in this model is described in Fu *et al.* (1995), which is based on the delta-four-stream approximation (Liou *et al.* 1988) in both solar and thermal infrared wavelengths.

c. Surface flux parameterization

At the lower boundary, the vertical turbulent fluxes of momentum, potential temperature and water vapor are determined by the surface-layer profiles of the wind velocity and the surface-layer potential temperature and water vapor according to the flux-profile relationships given by Deardorff (1972).

d. Turbulence parameterization

Turbulence parameterization currently used is a temporary one. Using the eddy viscosity coefficient K^M, we may write the turbulence terms in (2.8), (2.9) and (2.10) as

$$\left(\frac{\partial F_w}{\partial y}-\frac{\partial F_v}{\partial z}\right)\equiv\frac{1}{\rho_0}\frac{\partial}{\partial x}\left[\rho_0 K^M\frac{\partial(\rho_0\xi)}{\partial x}\right]+\frac{1}{\rho_0}\frac{\partial}{\partial y}\left[\rho_0 K^M\frac{\partial(\rho_0\xi)}{\partial y}\right]+\frac{1}{\rho_0}\frac{\partial}{\partial z}\left[\rho_0 K^M\frac{\partial(\rho_0\xi)}{\partial z}\right], \tag{4.1}$$

$$\left(\frac{\partial F_u}{\partial z}-\frac{\partial F_w}{\partial x}\right)\equiv\frac{1}{\rho_0}\frac{\partial}{\partial x}\left[\rho_0 K^M\frac{\partial(\rho_0\eta)}{\partial x}\right]+\frac{1}{\rho_0}\frac{\partial}{\partial y}\left[\rho_0 K^M\frac{\partial(\rho_0\eta)}{\partial y}\right]+\frac{1}{\rho_0}\frac{\partial}{\partial z}\left[\rho_0 K^M\frac{\partial(\rho_0\eta)}{\partial z}\right], \tag{4.2}$$

$$\left(\frac{\partial F_v}{\partial x}-\frac{\partial F_u}{\partial y}\right)\equiv\frac{1}{\rho_0}\frac{\partial}{\partial x}\left[\rho_0 K^M\frac{\partial(\rho_0\zeta)}{\partial x}\right]+\frac{1}{\rho_0}\frac{\partial}{\partial y}\left[\rho_0 K^M\frac{\partial(\rho_0\zeta)}{\partial y}\right]+\frac{1}{\rho_0}\frac{\partial}{\partial z}\left[\rho_0 K^M\frac{\partial(\rho_0\zeta)}{\partial z}\right]. \tag{4.3}$$

The turbulence terms in (2.11) for the potential temperature can also be written as

$$H=-\left[\frac{1}{\rho_0}\frac{\partial}{\partial x}\left(\rho_0\overline{u''\theta''}\right)+\frac{1}{\rho_0}\frac{\partial}{\partial y}\left(\rho_0\overline{v''\theta''}\right)+\frac{1}{\rho_0}\frac{\partial}{\partial z}\left(\rho_0\overline{w''\theta''}\right)\right]$$

$$= \frac{1}{\rho_0}\frac{\partial}{\partial x}\left[\rho_0 K^H \frac{\partial \theta}{\partial x}\right] + \frac{1}{\rho_0}\frac{\partial}{\partial y}\left[\rho_0 K^H \frac{\partial \theta}{\partial y}\right] + \frac{1}{\rho_0}\frac{\partial}{\partial z}\left[\rho_0 K^H \frac{\partial \theta}{\partial z}\right], \qquad (4.4)$$

where K^H is the eddy diffusivity.

Following Shutts and Gray (1994), we use

$$K^M = \lambda^2 \left\{ \left(R^\zeta\right)^2 + \left(R^\eta\right)^2 + \left(R^\xi\right)^2 + 2\left[\left(\frac{\partial u}{\partial x}\right)^2 + \left(\frac{\partial v}{\partial y}\right)^2 + \left(\frac{\partial w}{\partial z}\right)^2\right]\right\}^{1/2} F_M\left(Ri\right), \qquad (4.5)$$

$$K^H = \lambda^2 \left\{ \left(R^\zeta\right)^2 + \left(R^\eta\right)^2 + \left(R^\xi\right)^2 + 2\left[\left(\frac{\partial u}{\partial x}\right)^2 + \left(\frac{\partial v}{\partial y}\right)^2 + \left(\frac{\partial w}{\partial z}\right)^2\right]\right\}^{1/2} F_H\left(Ri\right), \qquad (4.6)$$

where

$$F_M\left(Ri\right) = \begin{cases} \left(1 - 16Ri\right)^{1/2} & Ri < 0 \\ \left(1 - 4Ri\right)^4 & 0 < Ri < 1/4 \\ 0 & Ri > 1/4 \end{cases}, \qquad (4.7)$$

and

$$F_H\left(Ri\right) = \begin{cases} 1.4\left(1 - 40Ri\right)^{1/2} & Ri < 0 \\ 1.4\left(1 - 1.2Ri\right)\left(1 - 4Ri\right)^4 & 0 < Ri < 1/4 \\ 0 & Ri > 1/4 \end{cases}. \qquad (4.8)$$

The dissipation length λ is given by

$$\frac{1}{\lambda^2} = \frac{1}{\lambda_0^2} + \frac{1}{\left[k\left(z + z_0\right)\right]^2}, \qquad (4.9)$$

where $\lambda_0 = C_s \Delta$, $C_s = 0.23$, Δ is the characteristic grid spacing, $k = 0.35$ is von Karman's constant and z_0 is the roughness length. The Richardson number is defined as

$$Ri = \frac{\left(\frac{g}{\theta}\frac{d\theta}{dz}\right)}{\left\{\left(R^\zeta\right)^2 + \left(R^\eta\right)^2 + \left(R^\xi\right)^2 + 2\left[\left(\frac{\partial u}{\partial x}\right)^2 + \left(\frac{\partial v}{\partial y}\right)^2 + \left(\frac{\partial w}{\partial z}\right)^2\right]\right\}}. \qquad (4.10)$$

The eddy viscosity and diffusivity coefficients, K^M and K^H, are defined at θ-points (see Figs. 1 and 2). Equation (4.5) is discretized as

$$
\begin{aligned}
K^M_{i,j,k} = (k_D\Delta)^2 \Bigg\{ & \frac{1}{4}\Big[\left(R^{\zeta}_{i-1/2,j-1/2,k}\right)^2 + \left(R^{\zeta}_{i-1/2,j+1/2,k}\right)^2 + \left(R^{\zeta}_{i+1/2,j-1/2,k}\right)^2 + \left(R^{\zeta}_{i+1/2,j+1/2,k}\right)^2\Big] \\
& + \frac{1}{4}\Big[\left(R^{\eta}_{i-1/2,j,k+1/2}\right)^2 + \left(R^{\eta}_{i+1/2,j,k+1/2}\right)^2 + \left(R^{\eta}_{i-1/2,j,k-1/2}\right)^2 + \left(R^{\eta}_{i+1/2,j,k-1/2}\right)^2\Big] \\
& + \frac{1}{4}\Big[\left(R^{\xi}_{i,j-1/2,k+1/2}\right)^2 + \left(R^{\xi}_{i,j+1/2,k+1/2}\right)^2 + \left(R^{\xi}_{i,j-1/2,k-1/2}\right)^2 + \left(R^{\xi}_{i,j+1/2,k-1/2}\right)^2\Big] \\
& + 2\left[\frac{\left(u_{i+1/2,j,k}-u_{i-1/2,j,k}\right)^2}{dx^2} + \frac{\left(v_{i,j+1/2,k}-v_{i,j-1/2,k}\right)^2}{dy^2} + \frac{m_k^2\left(w_{i,j,k+1/2}-w_{i,j,k-1/2}\right)^2}{dz'^2}\right]\Bigg\}^{1/2}.
\end{aligned}
\tag{4.11}
$$

The eddy vorticity flux convergence defined as in (4.1) is discretized as

$$
\begin{aligned}
& \left(\frac{\partial F_w}{\partial y} - \frac{\partial F_v}{\partial z}\right)_{i,j+1/2,k+1/2} \\
& \equiv \frac{1}{8dx^2}\Big[\left(K^M_{i,j,k}+K^M_{i+1,j,k}+K^M_{i,j+1,k}+K^M_{i+1,j+1,k}+K^M_{i,j,k+1}+K^M_{i+1,j,k+1}+K^M_{i,j+1,k+1}+K^M_{i+1,j+1,k+1}\right) \\
& \qquad \times\left((\rho_0\xi)_{i+1,j+1/2,k+1/2}-(\rho_0\xi)_{i,j+1/2,k+1/2}\right) \\
& \qquad -\left(K^M_{i-1,j,k}+K^M_{i,j,k}+K^M_{i-1,j+1,k}+K^M_{i,j+1,k}+K^M_{i-1,j,k+1}+K^M_{i,j,k+1}+K^M_{i-1,j+1,k+1}+K^M_{i,j+1,k+1}\right) \\
& \qquad \times\left((\rho_0\xi)_{i,j+1/2,k+1/2}-(\rho_0\xi)_{i-1,j+1/2,k+1/2}\right)\Big] \\
& + \frac{1}{2dy^2}\Big[\left(K^M_{i,j+1,k}+K^M_{i,j+1,k+1}\right)\left((\rho_0\xi)_{i,j+3/2,k+1/2}-(\rho_0\xi)_{i,j+1/2,k+1/2}\right) \\
& \qquad -\left(K^M_{i,j,k}+K^M_{i,j,k+1}\right)\left((\rho_0\xi)_{i,j+1/2,k+1/2}-(\rho_0\xi)_{i,j-1/2,k+1/2}\right)\Big] \\
& + \frac{m_{k+1/2}}{2\rho_{0,k+1/2}dz'^2}\Big[m_{k+1}\rho_{0,k+1}\left(K^M_{i,j,k+1}+K^M_{i,j+1,k+1}\right)\left((\rho_0\xi)_{i,j+1/2,k+3/2}-(\rho_0\xi)_{i,j+1/2,k+1/2}\right) \\
& \qquad -m_k\rho_{0,k}\left(K^M_{i,j,k}+K^M_{i,j+1,k}\right)\left((\rho_0\xi)_{i,j+1/2,k+1/2}-(\rho_0\xi)_{i,j+1/2,k-1/2}\right)\Big].
\end{aligned}
\tag{4.12}
$$

Similar discretizations are used for the eddy vorticity flux convergence in (4.2) and (4.3).

Next to the surface ($k = 1+1/2$), the vertical eddy flux convergences of ξ and η are discretized as

$$\frac{m_{1+1/2}}{2\rho_{0,1+1/2}dz'^2}\Big[m_2\rho_{0,2}\left(K^M_{i,j,2}+K^M_{i,j+1,2}\right)\left((\rho_0\xi)_{i,j+1/2,2+1/2}-(\rho_0\xi)_{i,j+1/2,1+1/2}\right)$$
$$-m_1\rho_{0,1}\left(K^M_{i,j,1}+K^M_{i,j+1,1}\right)\left((\rho_0\xi)_{i,j+1/2,1+1/2}-(\rho_0\xi)_{i,j+1/2,1/2}\right)\Big], \qquad (4.13)$$
$$+\frac{m_1 m_{1+1/2}}{\rho_{0,1}dz'^2}\left(\rho_0\overline{v''w''}\right)_{sfc}$$

$$\frac{m_{1+1/2}}{2\rho_{0,1+1/2}dz'^2}\Big[m_2\rho_{0,2}\left(K^M_{i,j,2}+K^M_{i+1,j,2}\right)\left((\rho_0\eta)_{i+1/2,j,2+1/2}-(\rho_0\eta)_{i+1/2,j,1+1/2}\right)$$
$$-m_1\rho_{0,1}\left(K^M_{i,j,1}+K^M_{i+1,j,1}\right)\left((\rho_0\eta)_{i+1/2,j,1+1/2}-(\rho_0\eta)_{i+1/2,j,1/2}\right)\Big], \qquad (4.14)$$
$$+\frac{m_1 m_{1+1/2}}{\rho_{0,1}dz'^2}\left(\rho_0\overline{u''w''}\right)_{sfc}$$

respectively.

The eddy potential temperature flux convergence, H, defined as in (4.4), is discretized as

$$H_{i,j,k}=\frac{1}{2dx^2}\Big[\left(K^H_{i+1,j,k}+K^H_{i,j,k}\right)\left(\theta_{i+1,j,k}-\theta_{i,j,k}\right)-\left(K^H_{i,j,k}+K^H_{i-1,j,k}\right)\left(\theta_{i,j,k}-\theta_{i-1,j,k}\right)\Big]$$
$$+\frac{1}{2dy^2}\Big[\left(K^H_{i,j+1,k}+K^H_{i,j,k}\right)\left(\theta_{i,j+1,k}-\theta_{i,j,k}\right)-\left(K^H_{i,j,k}+K^H_{i,j-1,k}\right)\left(\theta_{i,j,k}-\theta_{i,j-1,k}\right)\Big]$$
$$+\frac{m_k}{2\rho_{0,k}dz'^2}\Big[m_{k+1/2}\rho_{0,k+1/2}\left(K^H_{i,j,k+1}+K^H_{i,j,k}\right)\left(\theta_{i,j,k+1}-\theta_{i,j,k}\right)$$
$$-m_{k-1/2}\rho_{0,k-1/2}\left(K^H_{i,j,k}+K^H_{i,j,k-1}\right)\left(\theta_{i,j,k}-\theta_{i,j,k-1}\right)\Big]. \qquad (4.15)$$

Next to the surface ($k=1$), the vertical eddy flux convergence of θ is shown as

$$\frac{m_1}{2\rho_{0,1}dz'^2}\Big[m_{1+1/2}\rho_{0,1+1/2}\left(K^H_{i,j,2}+K^H_{i,j,1}\right)\left(\theta_{i,j,2}-\theta_{i,j,1}\right)\Big]+\frac{m_1}{\rho_{0,1}dz'}\left(\rho_0\overline{\theta''w''}\right)_{sfc}. \qquad (4.16)$$

The eddy flux convergence of water vapor is discretized in a way similar to (4.15) and (4.16).

5. Additional modeling aspects

a. Boundary conditions

The properties of the underlying surface required by the model are temperature, wetness, and roughness length. Currently, all three are prescribed. The upper and lower boundaries are rigid horizontal planes. The horizontal components of vorticity are fixed to zero at the upper and lower boundaries. The diffusive upward fluxes are zero at the upper boundary. The horizontal boundary condition is cyclic.

b. Time differencing

In this model, the second-order Adams-Bashforth scheme is used except that the first-order backward scheme is used for the buoyancy and turbulence terms and the first-order forward scheme is used for the physics terms.

c. Realizability

The variables q_c, q_i, q_r, q_s, and q_g are checked for negative values. Based on the assumption that negative values of theses quantities are primarily due to computational dispersion, we use an algorithm to "fill" the "holes", which conserves the domain integral (Krueger, 1988). The first step is to take from the 26 adjacent grid points. Each of these points is "taxed" proportional to its value if its value is positive. If "taxes" from the surrounding points cannot fill the "hole", the remaining amount needed to fill it is taken from the rest of the points, again proportional to each point's value. If there are many nearby "holes", a non-"hole" point may be "overtaxed" and become a "hole". This is allowed. This procedure is repeated until all the "holes" have been filled.

d. Other components of model physics

The model includes a Newtonian-type cooling above the 10-km height and a Rayleigh-type friction in the top 5 layers.

6. Experiments without physics

We have performed a series of idealized experiments to simulate the time evolution of thermals in various environmental conditions. The main purpose of these experiments is to demonstrate the computational performance of the dynamics core of the model as well as to gain better understanding of basic convective processes from the viewpoint of vorticity dynamics.

All experiments described in this section are performed without model physics and Coriolis force. A 250-m grid size and a 32-km $\times$ 32-km horizontal domain are used. The vertical grid size is 250 m and the vertical domain is 15-km deep or 30-km deep depending on the experiments. (The stretched vertical grid described in section 3b is not used in these idealized experiments.) The initial thermodynamic state is isentropic up to the 15-km height. An isothermal layer is included above that height in some of the experiments. The initial motion fields are taken from a short-term (5 minutes) pre-simulation of an ellipsoidal buoyant thermal. In most of the experiments, a weak linear diffusion is applied to the vorticity components and potential temperature. The time step used is 10 seconds.

a. EXP1 and EXP2

These experiments are designed to compare the performance of advection schemes used in the model. Two experiments are carried out with different values of α in (3.22) for vorticity advection: EXP1 uses an enstrophy-conserving 2nd-order scheme with $\alpha = 0$ and EXP2 uses an enstrophy-bounded partially 3rd-order scheme with $\alpha = 1$. Except for the advection scheme, simulation conditions for EXP1 and EXP2 are identical. The vertical domain is 15-km deep. An ellipsoidal form of potential temperature perturbation and associated axisymmetric motion fields are initially given to the resting basic state. Since there is no shear, the solution should remain approximately axisymmetric in time. (Because we use a square grid with cyclic boundary conditions, the

axisymmetry cannot be maintained exactly.) The x-z cross sections of those fields at the center of the y-domain are shown in Fig. 5.

In these experiments, neither buoyancy nor diffusion is included. The initial vorticity field is, therefore, simply advected by wind, with possible stretching/ shrinking effects in the azimuthal direction.

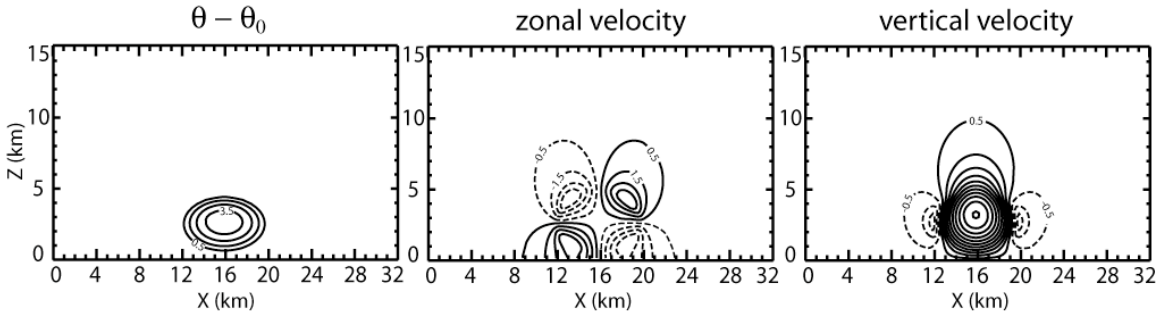

Fig. 5. Initial conditions for EXP1 and EXP2: x-z cross-sections of (left) potential temperature perturbation and (middle) zonal and (right) vertical velocities at the center of y-domain. Ordinary and dashed lines represent positive and negative values, respectively. Contour intervals are (left) 1-K and (middle and right) 1-ms^{-1}.

Figure 6 shows the potential vorticity fields simulated by EXP1 and EXP2. Here, potential vorticity is defined as the azimuthal component of vorticity divided by density and the distance from the axis of axisymmetry. This quantity is supposed to be conserved with respect to a material element for an axisymmetric flow when time is continuous. As the left column of Fig. 6 shows, the potential vorticity field becomes increasingly noisy with time in EXP1. Even though the 2nd-order scheme conserves enstrophy and, therefore, has a good control of nonlinear computational instability (Arakawa and Lamb, 1977), it is subject to serious dispersion errors as shown in the figure. As the right column of Fig. 6 shows, on the contrary, such dispersion errors are drastically reduced in EXP2 with the partially 3rd-order scheme.

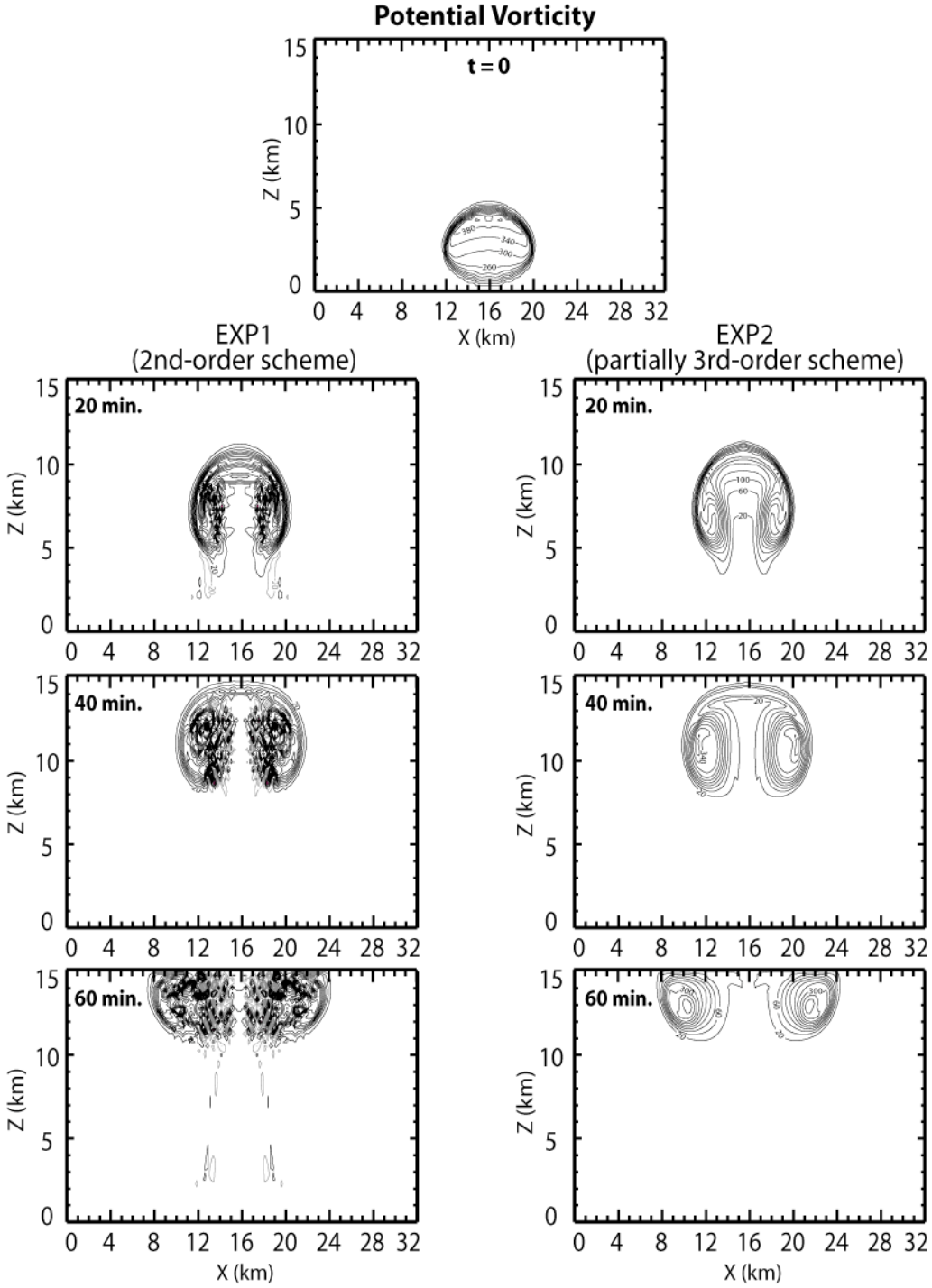

Fig. 6. Time evolution of the simulated potential vorticity fields on x-z cross-section at the center of y-domain obtained from (left) EXP1 and (right) EXP2. Contour interval is 40×10^{-4} s^{-1}. Gray lines represent negative values.

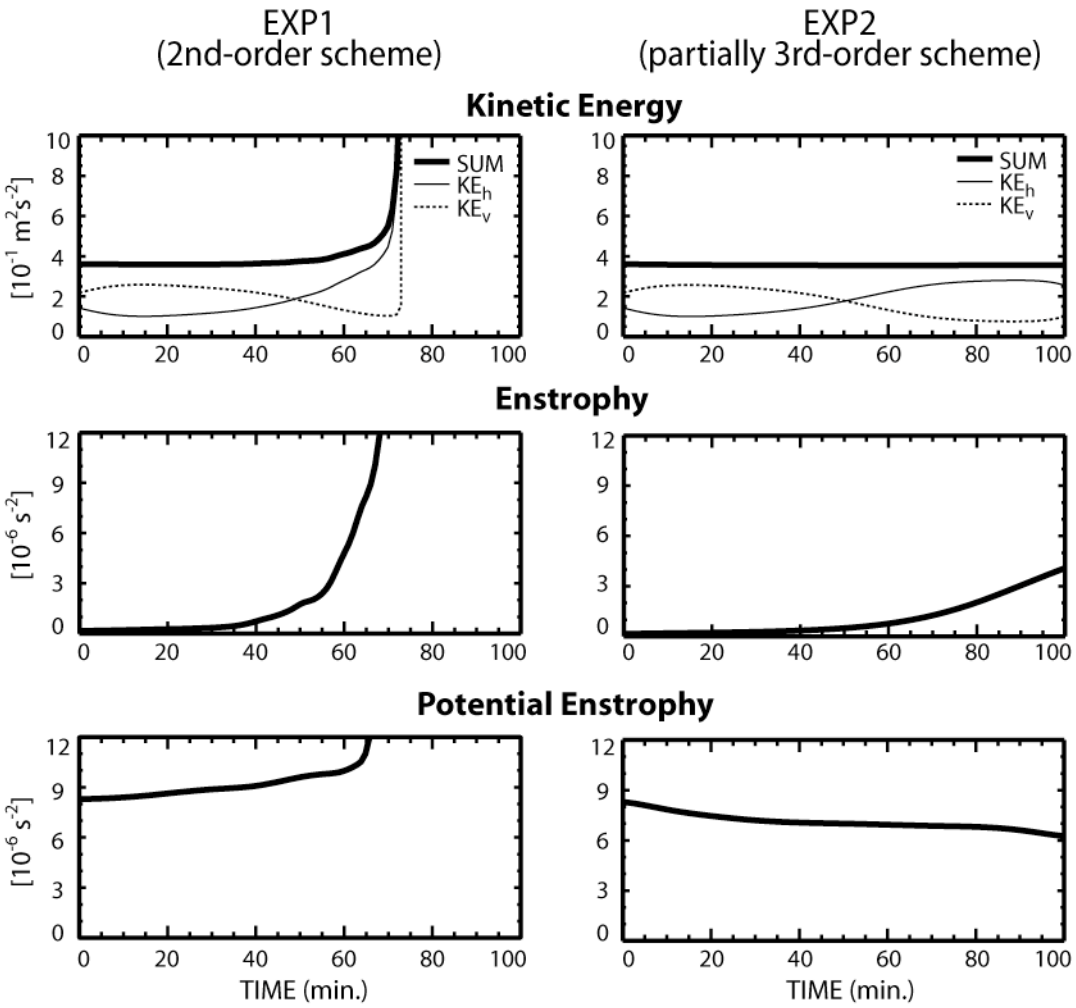

Fig. 7. The mass-weighted three-dimensional domain-averaged (upper) kinetic energy, (middle) enstrophy, and (lower) potential enstrophy obtained from (left) EXP1 and (right) EXP2. In the upper panels, thin ordinary, dotted, and thick lines represent horizontal and vertical components of kinetic energy and their sum, respectively.

In Fig. 7, we show the mass-weighted three-dimensional domain-averaged kinetic energy, enstrophy, and potential enstrophy as functions of time. With the 2nd-order scheme, the kinetic energy and potential enstrophy are approximately conserved only in the early stage of the experiment, increasing exponentially afterwards. With the partially 3rd-order scheme, on the other hand, the kinetic energy is practically conserved throughout the experiment while the potential enstrophy slowly decreases in time. The relatively rapid decreases near the beginning and end of the experiments are due to the existence of small-scale components in the initial condition and the generation of those components by

the complex interference between the approximately axisymmetric flow and the square geometry of the domain, respectively. In contrast to the potential enstrophy, the enstrophy increases with time. Since both the kinetic energy and potential enstrophy are practically conserved, we believe that this increase of the enstrophy is physical.

Through EXP1 and EXP2, it is demonstrated that the partially 3rd-order enstrophy-bounded advection scheme effectively controls computational noise by keeping dispersion errors small. Our results are consistent with earlier studies with 3rd-order schemes (e.g. Takacs, 1985; Leslie and Dietachmayer, 1997).

b. EXP3 and EXP3S

To test the performance of the model for purely three-dimensional situations and understand some of the basic interactions between a thermal and a basic flow, two experiments are performed: EXP3 initially with no basic flow and EXP3S initially with a horizontally uniform basic flow in the x direction with vertical shear. The initial conditions for the thermal are shown in Fig.8. Unlike EXP1 and EXP2, both the buoyancy and diffusion terms are included and thus a rather weak initial potential temperature perturbation is used. The vertical domain is again 15-km deep. For EXP3S, horizontally uniform westerly wind (u_0) that linearly increases from 0 at the surface to 10 m s^{-1} at 15-km height is added to the initial wind field.

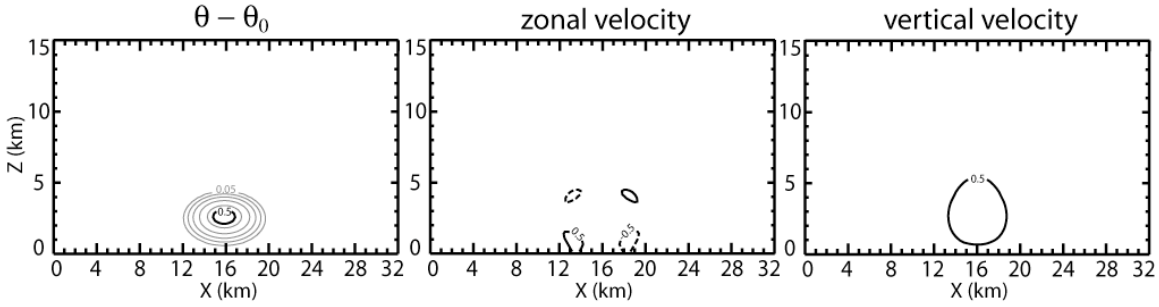

Fig. 8. As in Fig. 5 but for EXP3 and EXP3S. Contour interval of gray lines in the left panel is 0.1-K.

In these simulations, the initial thermal near the surface rises due to the buoyancy in the neutral atmosphere until it reaches the upper boundary. With the shear in the basic flow, the thermal is slanted with height and thus its axisymmetry is not maintained even approximately. To examine the motion field associated with the thermal further, Fig. 9 shows the y-component of vorticity (η) on the x-z cross-section at the center of the y-domain obtained from EXP3 (upper) and EXP3S (lower). Blue line represents negative value. The updraft and downdraft are shaded with yellow and light blue, respectively. In the lower panels (EXP3S), the initial vorticity due to the shear of the basic flow, η_o $\left(\equiv \rho_0^{-1}\partial u_0/\partial z\right)$, is subtracted. In the figure, it can be seen that without shear, positive (clockwise) and negative (counter-clockwise) vortices symmetrically develop around the updraft. With shear, on the contrary, asymmetry appears between the positive and negative vortices due to the downward stretching of the negative vortex at the upwind side and the upward shrinking of the positive vortex at the downwind side. Thus it is clear that the net vertical transport of η is zero in EXP3 and dominantly positive (upward) in EXP3S. As we show quantitatively later through (7.1), the upward transport of η means deceleration of the westerly flow.

The corresponding zonal wind field obtained from EXP3S is shown in Fig. 10. Here, the initial basic flow (u_0) is subtracted. It can be clearly seen that the zonal wind is decelerated primarily in the active updraft/downdraft regions.

Figure 11 shows *horizontal* cross sections of the vertical component of vorticity (ζ, upper) and the zonal wind (u, lower) at 5-, 8- and 13-km heights from EXP3S. In the figure, we see that positive vorticity (counter-clockwise in the figure) develops on the right side of the updraft relative to the shear vector. On the left side of the updraft, on the other hand, negative vorticity (clockwise) develops. Similar vorticity couplets associated with cloud clusters in shear flow have been observed by many authors (e.g. Schlesinger, 1980; Cho and Clark, 1981; Rotunno, 1981; Klemp et al., 1981; Tollerud and Esbensen, 1983). The zonal wind field shows corresponding local deceleration in the active updraft/downdraft regions and compensating acceleration in convectively inactive regions.

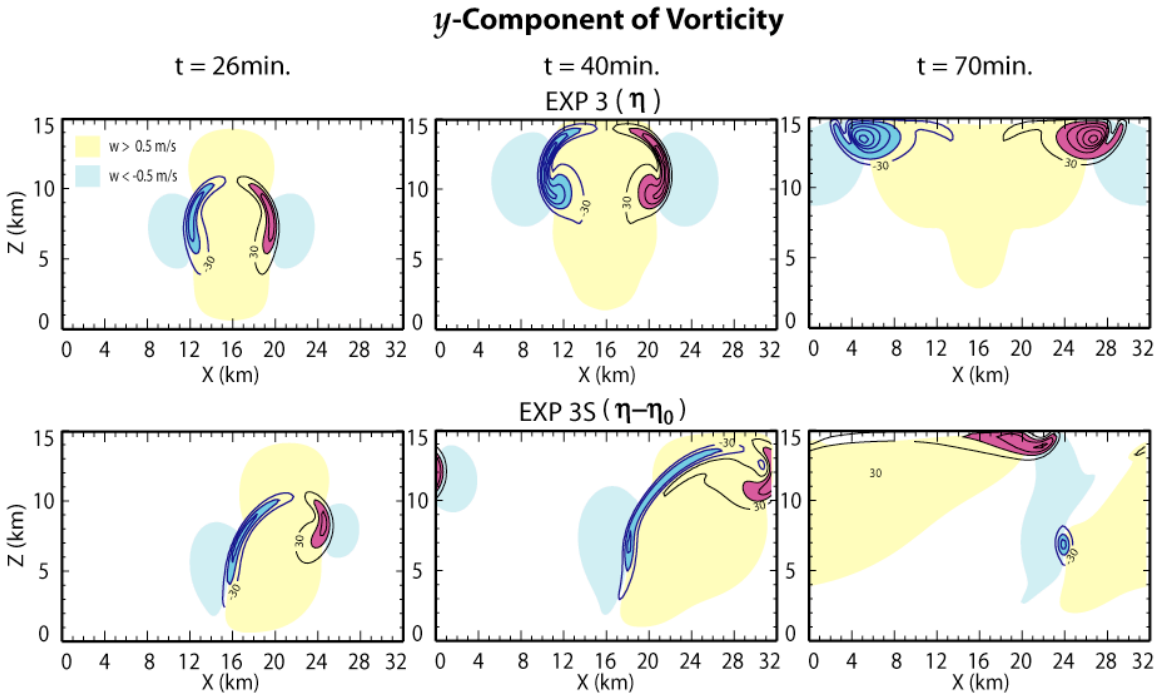

Fig. 9. The y-component of vorticity on x-z cross-section at the center of y-domain obtained from (upper) EXP3 and (lower) EXP3S. Black and blue lines represent positive and negative values, respectively. Contour interval is 60×10^{-4} $m^3kg^{-1}s^{-1}$. The updraft and downdraft are shaded with yellow and light blue, respectively.

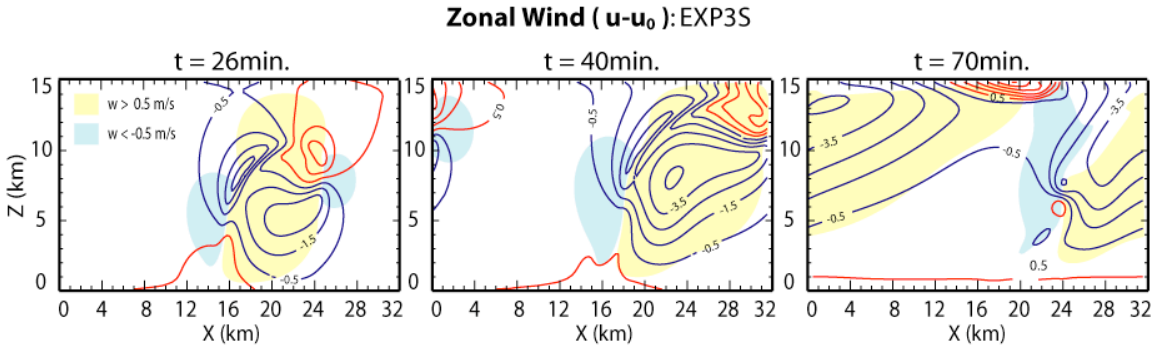

Fig. 10. Zonal wind on x-z cross-section at the center of y-domain obtained from EXP3S. The initial basic flow (u_0) is subtracted from the field. Red and blue lines represent positive and negative values, respectively. Contour interval is 1 ms^{-1}. The updraft and downdraft are shaded with yellow and light blue, respectively.

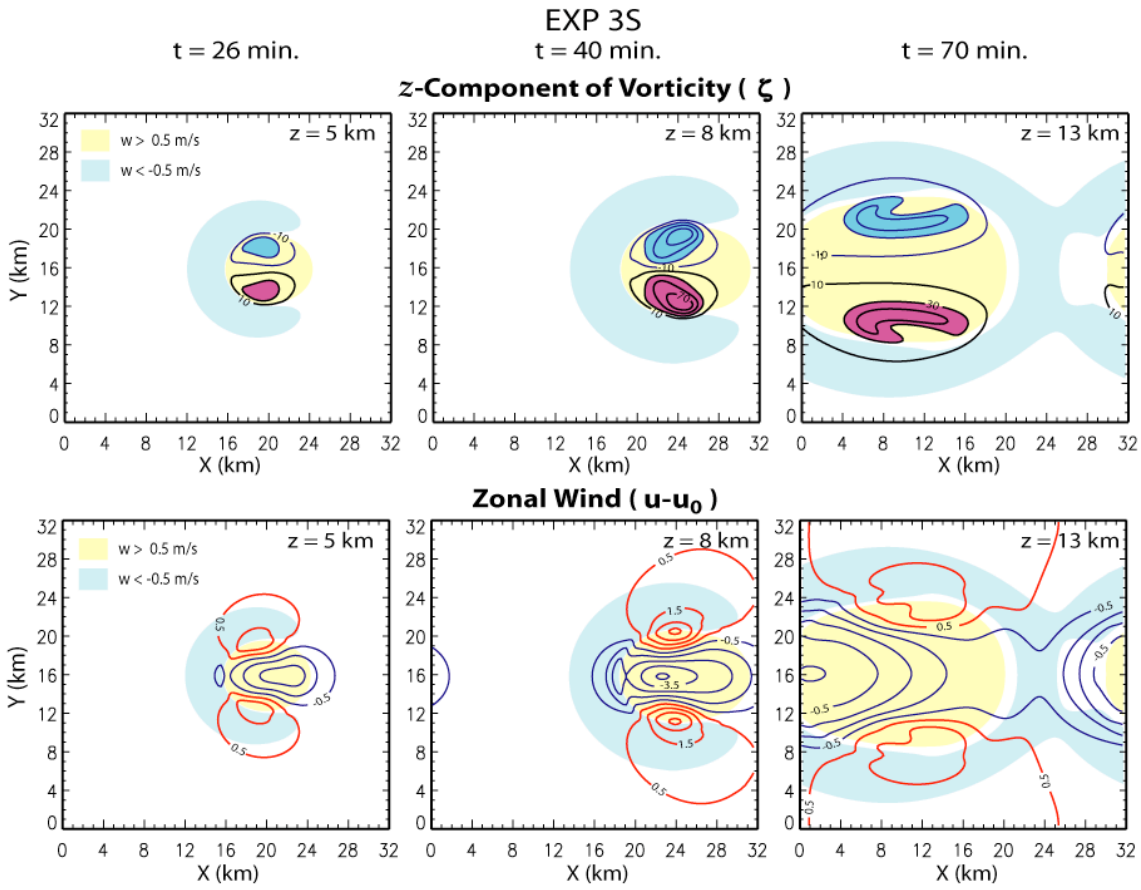

Fig. 11. The (upper) z-component of vorticity and (lower) zonal wind on x-y cross-section obtained from EXP3S. Red and black lines represent positive value and blue line represents negative value. Contour intervals are (upper) 20×10^{-4} $m^3kg^{-1}s^{-1}$ and (lower) 1 ms^{-1}. The updraft and downdraft are shaded with yellow and light blue, respectively.

The deceleration/acceleration patterns shown in the lower panels of Fig. 11 have pronounced structures in y. To further investigate such y-dependencies in a concise way, we show the x-averages of the three components of wind (left) and vorticity (right) for t=26 min on a y-z plane in Fig. 12. In the figure, blue line represents negative value. The x-component of vorticity (ξ) in Fig. 12d shows a direct circulation generated by the buoyancy associated with the thermal. It is consistent with the lower-level convergence and upper-level divergence in the y-component of wind (Fig. 12b) and the updraft at the center of the y-domain (Fig. 12c). Unlike the ξ-field, the y-component of vorticity ($\eta - \eta_0$) in Fig. 12e shows a vertical arrangement of positive and negative values. This is consistent with the asymmetry of the positive and negative vortices shown in the lower-left panel of

Fig. 9. Along with the couplet of the z-component of vorticity (ζ) shown in Fig.12f, the vertical arrangement of η-field is also consistent with the deceleration of zonal wind that has a maximum around the 5 km height.

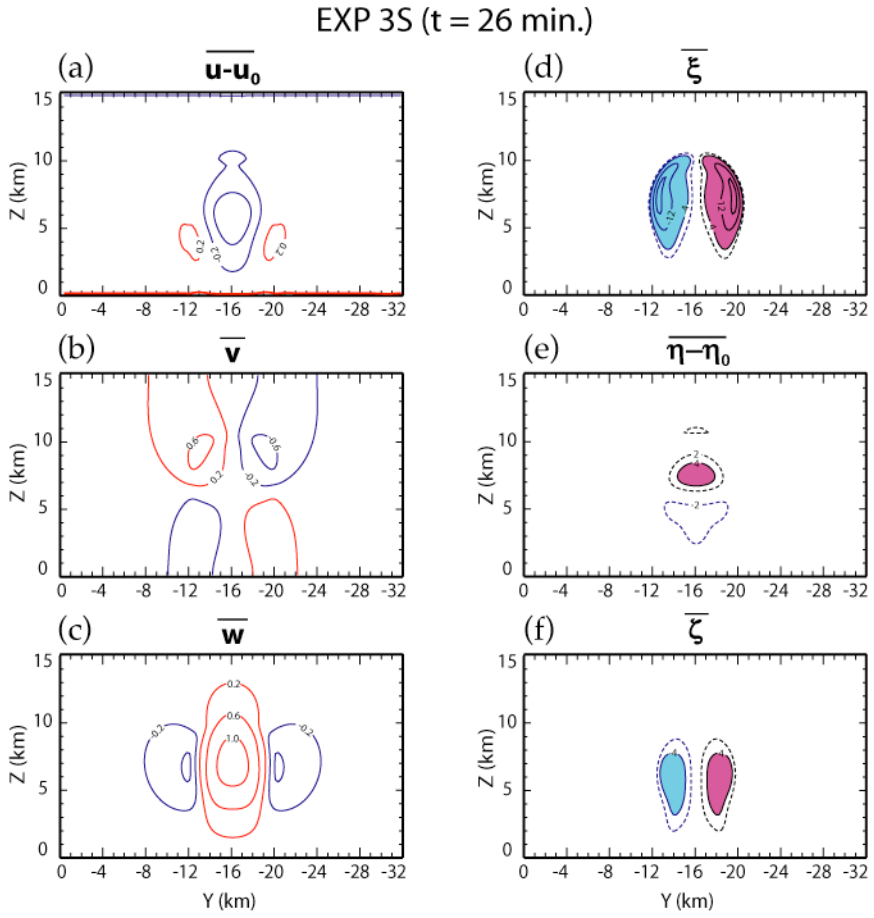

Fig. 12. Zonally averaged (a) zonal, (b) meridional and (c) vertical winds and (d) x-, (e) y- and (f) z-components of vorticity on y-z cross-section obtained from EXP3S at t=26min. Red and black lines represent positive value and blue line represents negative value. Contour interval in the wind fields is 0.4 ms^{-1}. Contours in the vorticity fields are ±2, ±4, ±12, ±20 … (10^{-4} $m^3kg^{-1}s^{-1}$).

As shown in Fig. 12, the motion field associated with the thermal is fully three-dimensional and all of the three components of vorticity are involved when there is a shear in the basic flow. The time change of vorticity depends on the flux convergence (divergence), stretching and twisting, diffusion, and buoyancy effects. Among these, dominant individual effects for the generation of the vorticity fields shown in Fig. 12 are plotted in Fig. 13a and the net effects in Fig. 13b. Theses are accumulated effects from t=0 to t=26 minutes. The figure shows

that the main source term for the generation of the ξ-field is the buoyancy. For the η- and ζ-fields, the twisting term is the main source. Circulation carries the generated ξ and ζ from the lower levels to the upper levels and η inward and upward through the flux convergence and divergence, respectively.

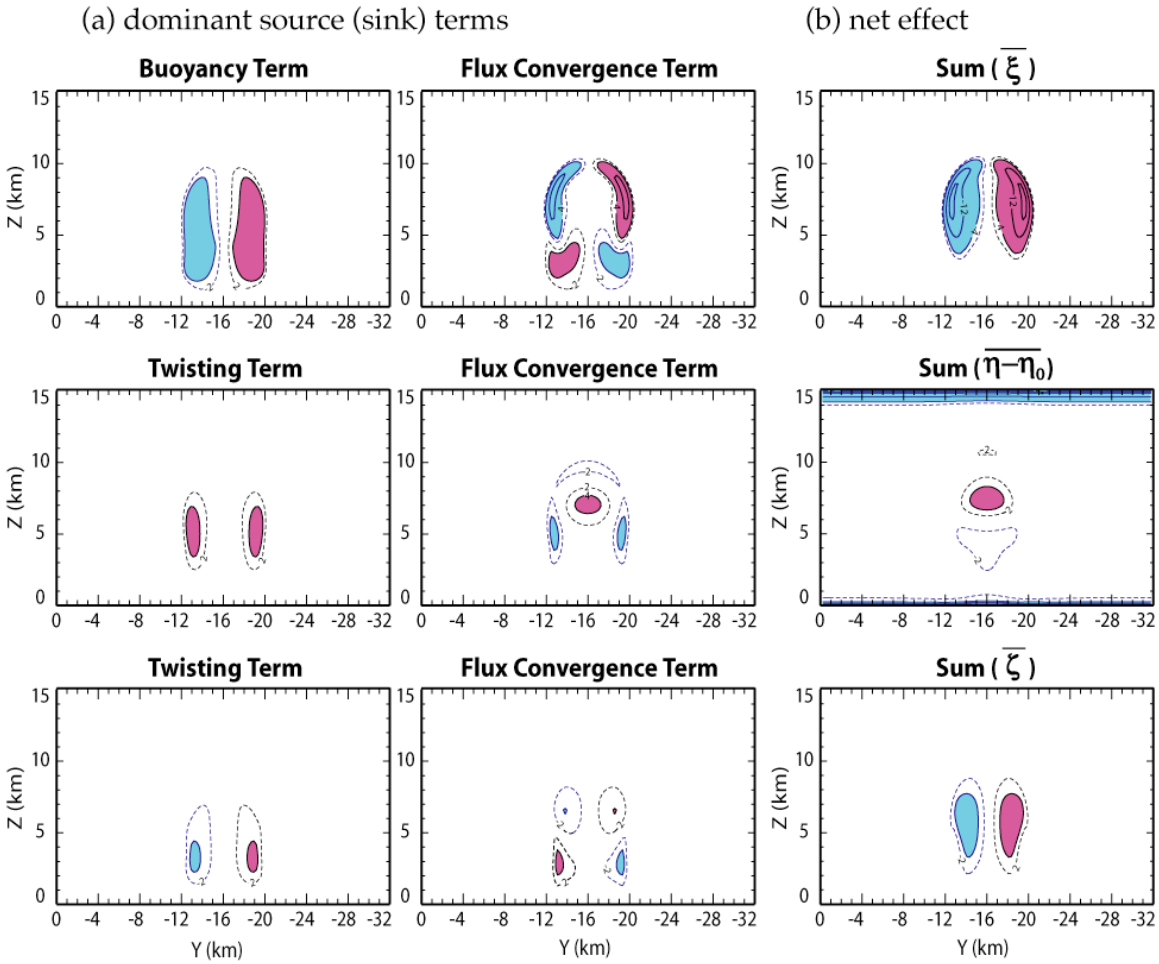

Fig. 13. Zonally averaged (a) dominant source (sink) terms and (b) net effect to generate (upper) x-, (middle) y-, and (lower) z-components of vorticity obtained from EXP3S. Black and blue lines represent positive and negative values, respectively. Contours are ±2, ±4, ±12, ±20 … (10^{-4} $m^3kg^{-1}s^{-1}$).

So far, the simulated results from EXP3S are interpreted in view of the three-dimensional vorticity dynamics, which governs the redistribution and reorientation of the three-dimensional vorticity vector and the associated change of the velocity fields. Figure 14, on the other hand, shows a diagnosis based on

the more standard viewpoint of the momentum dynamics. In this figure, the zonal averages of the vertical and zonal winds and the vertical eddy momentum flux from EXP3S are presented on z-t cross sections (upper panels) at the center of the y-domain. With time, the thermal rises and strong updraft appears at the upper levels. It is seen that the mean zonal wind decelerates in the updraft region and slightly accelerates near the surface. Thus the momentum is transported downward by the thermal as the lower panel shows. The deceleration means that the thermal behaves as a barrier to the mean flow.

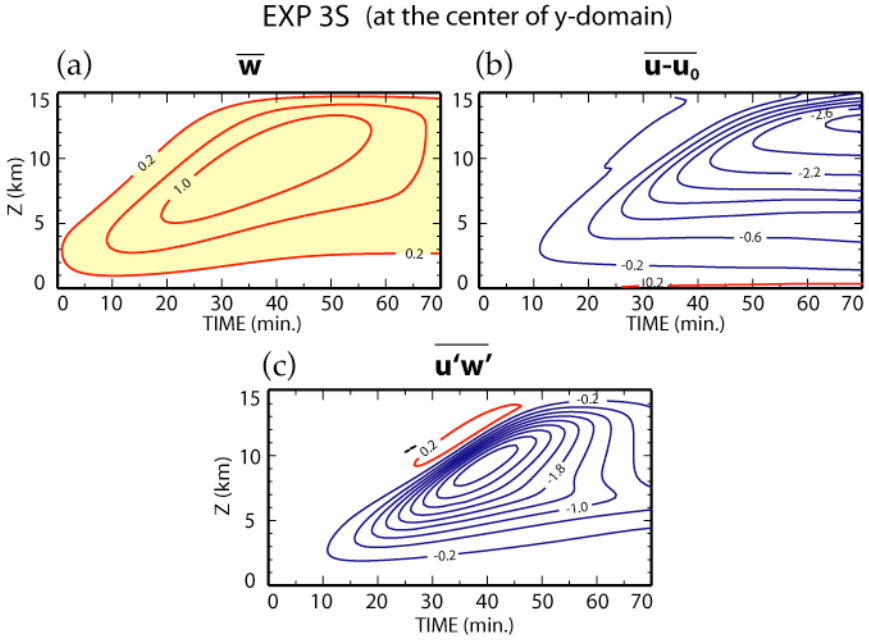

Fig. 14. Zonally averaged (a) vertical and (b) zonal components of wind and (c) vertical eddy momentum flux on z-t cross-section at the center of y-domain obtained from EXP3S. Red and blue lines represent positive and negative values, respectively. Contour intervals are (upper) 0.4 ms^{-1} and (lower) 0.4 m^2s^{-2}.

c. EXP4 and EXP4S

Theses experiments are essentially the same as EXP3 and EXP3S except for the inclusion of an extended vertical domain of 30 km deep. The initial conditions from the surface to 15-km height are the same as those in EXP3 and EXP3S.

Above the 15-km height, the model atmosphere is initially isothermal with no shear in the basic flow.

The differences between EXP4 and EXP3 and those between EXP4S and EXP3S are minor in general and thus we show only the y-components of the vorticity on the x-z cross-section at the center of the y-domain (Fig. 15). Below the 15-km height, the fields look hardly different from those in Fig. 9. Above that height, we see propagating gravity waves generated by the rising thermal. With a shear in the basic flow (EXP4S), gravity waves in the upper layer are tilted toward the upwind side. If theses waves are stationary in the x-direction, the tilt is an indication that the momentum is transferred downward. This feature is consistent with the result shown in Fig. 14.

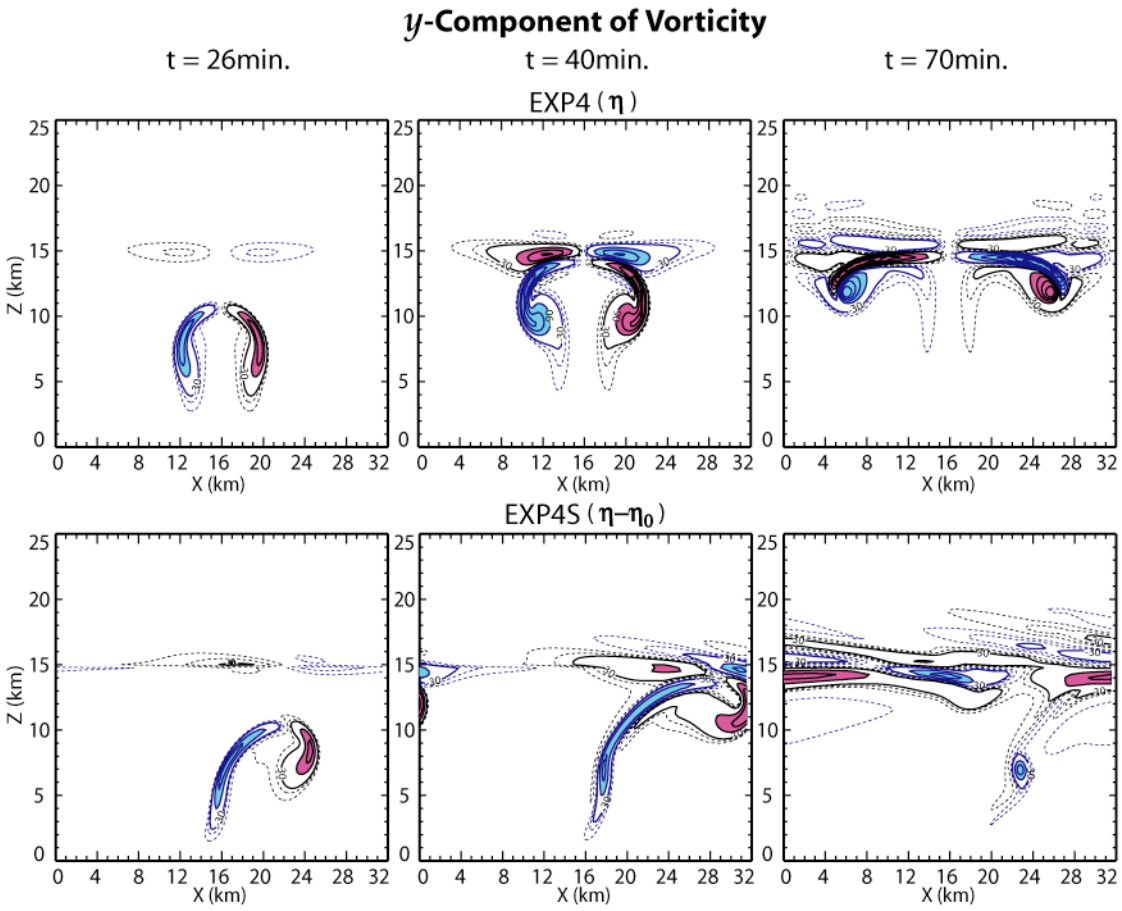

Fig. 15. As in Fig. 9 but obtained from (upper) EXP4 and (lower) EXP4S. Contour interval is 60×10^{-4} $m^3kg^{-1}s^{-1}$. Black and blue lines represent positive and negative values, respectively. Dotted lines are ±10 and ±20 (10^{-4} $m^3kg^{-1}s^{-1}$).

7. Experiment with physics

In this experiment called EXP5S, we simulate the development of an ensemble of clouds using the model with full physics, which includes microphysics, radiation, and turbulence. The model is applied to a 512-km × 512-km horizontal domain with a 2-km horizontal grid size. In the vertical, the model has 34 levels based on the stretched vertical grid described in section 3b with a top at 18 km. The vertical grid size ranges from about 100 m near the surface to about 1000 m near the model top. The upper and lower boundaries are rigid and the lateral boundaries are cyclic. The Coriolis parameter for 15° N is used. The model also includes a Newtonian-type cooling above the 10-km height to maintain realistic climatology of the stratosphere and a Rayleigh-type friction in the top 5 layers to absorb upward-propagating gravity waves.

An idealized ocean surface condition is used, in which the surface temperature is prescribed as 299.8 K. The cosine of the solar zenith angle is fixed to 0.5, representing a typical daytime condition in the tropics. The initial thermodynamic state and zonal wind fields are selected idealizing the GATE Phase-III conditions. Figure 16 shows the initial profiles of moist static energy and zonal wind. The meridional wind is initially set to zero. In order to maintain the mean wind shear, the area mean of zonal wind is fixed to its initial value throughout the simulation.

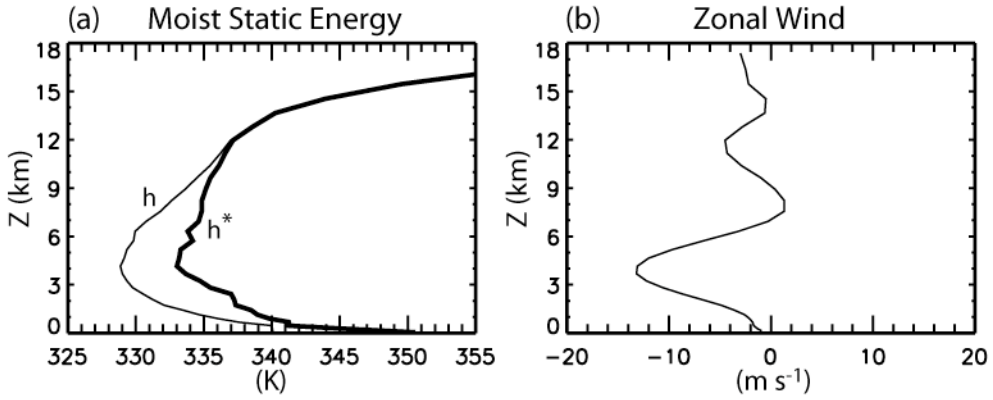

Fig. 16. Initial profiles of (a) moist static energy (h*; saturation moist static energy) divided by c_p and (b) zonal wind used in EXP5S, where c_p is the specific heat of dry air.

Clouds are initiated by small random potential temperature perturbations introduced into the lowest model layer over the 15-minute period after the first 5 minutes of the integration. Large-scale forcing representing climatological background is imposed on the model through prescribed cooling and moistening rates (Fig. 17). The integration period is 3 days and the time step is 10 seconds.

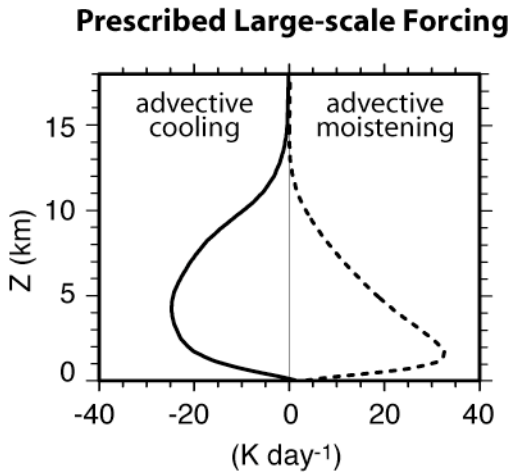

Fig. 17. Vertical profiles of the prescribed large-scale advective cooling and moistening rates used in EXP5S. Here, the moistening rate is multiplied by L/c_p, where L is the latent heat of condensation.

Analysis of EXP5S is in progress. In this technical report, only snapshots showing initial development are presented. Development of cloud ensemble for the initial 24-hour period can be seen in Fig. 18. The figure shows the isotimic surface of cloud water mixing ratio (q=0.1 $g\,kg^{-1}$) in every 6 hours. Here cloud water consists of cloud liquid water and cloud ice. In early stage of this period, clouds develop nearly everywhere because the integration starts from a horizontally uniform and conditionally unstable condition. As time progresses, mesoscale band-like cloud organizations gradually develop, which seem to have multiple directions.

Figure 19 shows the distribution of the cloud top temperature in the x-y domain in every 6 hours. Following Xu and Krueger (1991), the cloud top is defined as the layer where the path of liquid water and ice (i.e., $\int (q_c + q_i)\rho dz$) first exceeds 0.1 kg m^{-2} when integrated downward from the model top, where

q_c is the mixing ratio of cloud liquid water and q_i is that of ice. In the figure, cirrus anvils associated with cumulonimbi appear white and there are no clouds in black areas. As already seen in Fig. 18, several organized systems have developed during the last 12 hours of the 1-day simulation, which are consist of narrow convective bands mostly aligned in the 45°-angle against the direction of shear. Behind the bands, there are broad areas of midlevel stratiform clouds.

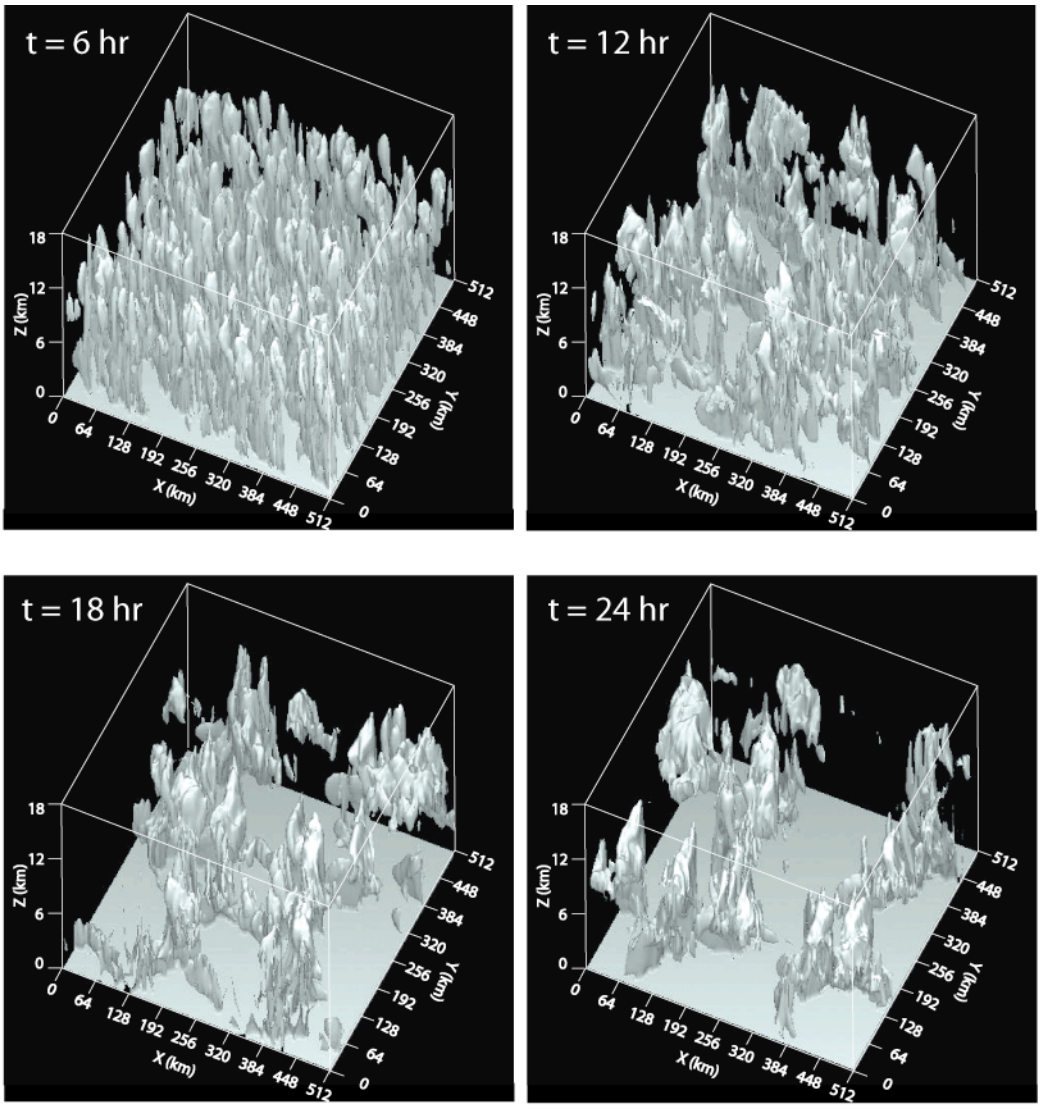

Fig. 18. Time evolution of isotimic surface of cloud water mixing ratio (0.1 gkg^{-1}) obtained from EXP5S, where the cloud water consists of cloud liquid water and cloud ice.

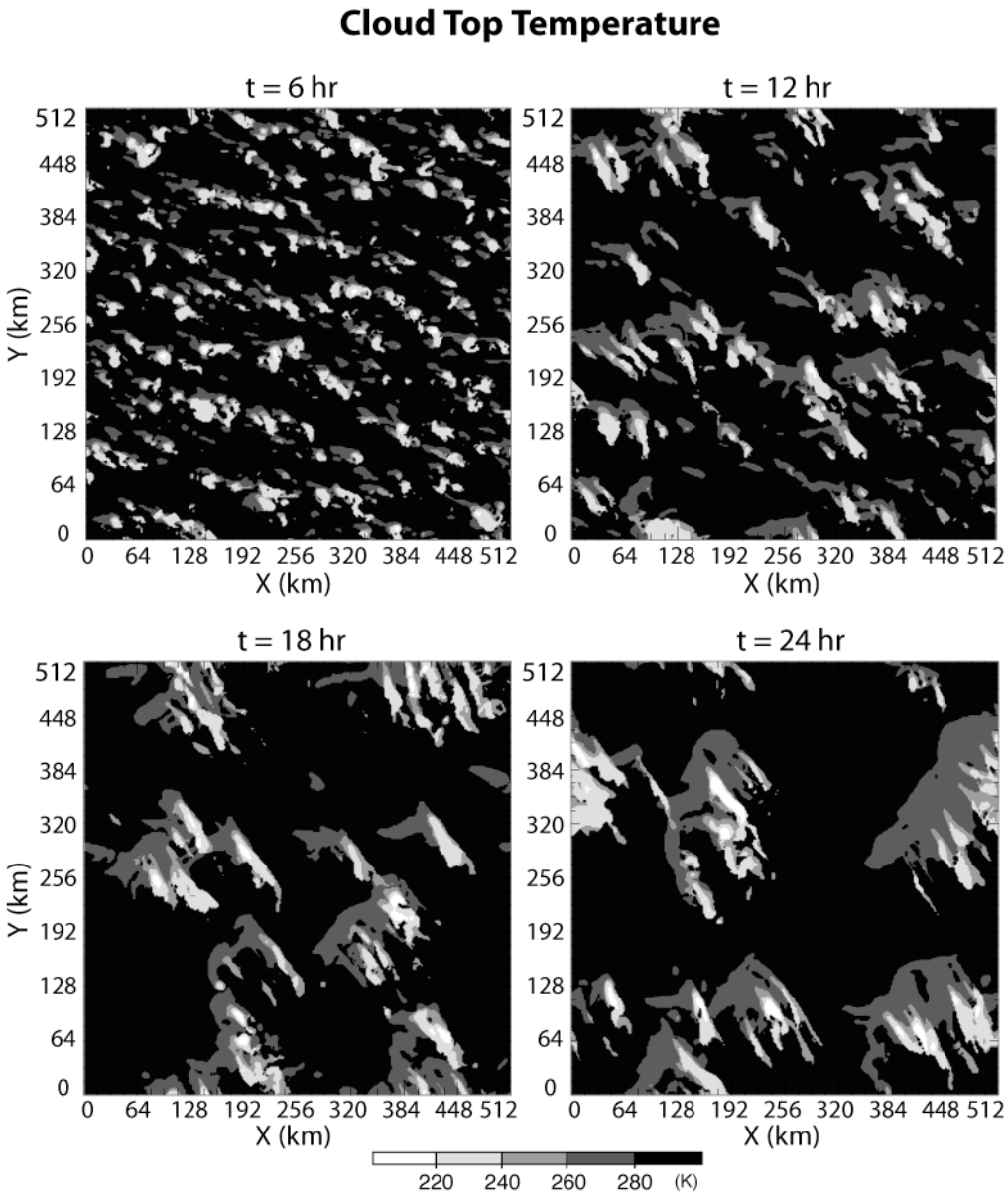

Fig. 19. Time evolution of cloud top temperature in the x-y domain obtained from EXP5S.

The domain- and time-averaged profiles of the vertical flux convergence of zonal momentum and the fluxes of vorticity components due to cumulus convection are shown in Fig. 20. Here, the time average is taken over the last 12 hours of the 1-day simulation. Figure 20a shows a layer of the westerly momentum flux convergence above the level of the mid-tropospheric easterly jet core shown in Fig. 16b, and a layer of easterly momentum flux convergence below the jet core. Although our experiment is highly idealized, especially

because the mean zonal wind and large-scale forcing are fixed in time to represent only the mean GATE Phase III condition, the result is consistent with those by Sui and Yanai (1986) and Mapes and Wu (2001).

With the use of the definition of vorticity (2.6), the anelastic continuity equation (2.1) and the cyclic continuity, the domain-averaged vertical flux convergence of zonal momentum can be expressed as

$$-\frac{\partial}{\rho_0 \partial z}\left(\rho_0 \overline{u'w'}\right) = -\rho_0 \overline{w'\eta'} + \rho_0 \overline{v'\zeta'}, \qquad (7.1)$$

where the over bar and prime indicate the domain average and deviation, respectively. Figure 20b shows the vorticity fluxes that appear in the right hand side of (7.1). When the y-component of vorticity is transported upward (downward), there is a deceleration (acceleration) tendency of westerly wind. The relation (7.1) gives an alternative way of viewing the cumulus momentum flux problem as a problem of vorticity transports by cumulus convection, which can be more straightforward since the effect of the perturbation pressure does not need to be explicitly formulated.

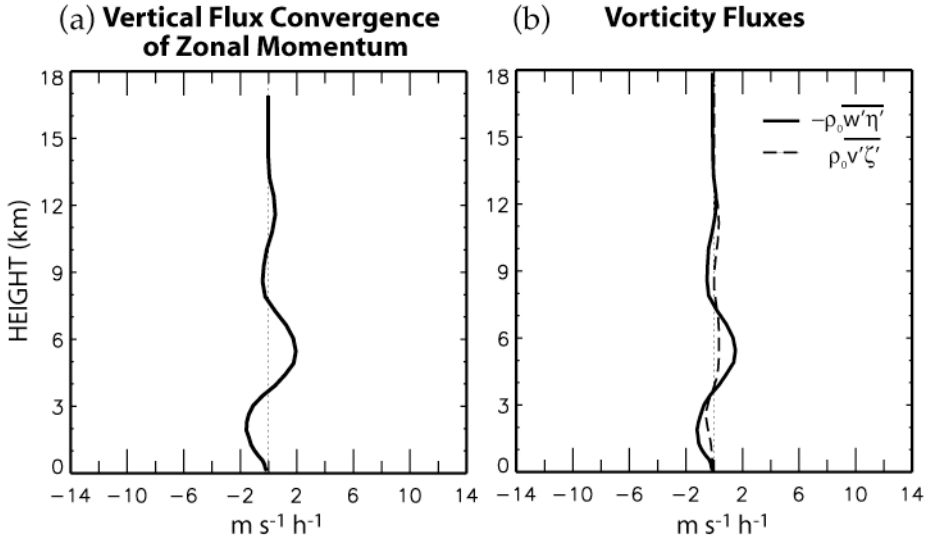

Fig. 20. Domain– and time-averaged profiles of (a) the vertical flux convergence of zonal momentum and (b) the fluxes of vorticity components due to cumulus convection obtained from EXP5S. The time average is taken over the last 12 hours of the 1-day simulation.

8. Summary

In this technical report, we present a detailed description of a newly developed three-dimensional anelastic cloud model. All of the three-dimensional cloud models developed so far view convective motions in terms of the pressure gradient and buoyancy forces in the momentum equation. The model described here is unique among its own kind because it is built on the dynamical framework of the three-dimensional vector vorticity equation instead.

The advantage of using the vorticity equation is that, by eliminating the passive pressure gradient terms, it leads us to examine convective motions directly in terms of the relevant dynamics such as generation, advection, stretching and twisting of the vorticity. Therefore, interpretation of the results can be more straightforward with the explicit use of the vorticity equation in the model. It is especially advantageous from the viewpoint of computational design because computational constraints on the key dynamical processes, such as those on enstrophy cascade under advection processes, can be more easily implemented into the system. In spite of theses advantages, the vorticity-equation system has so far been adopted as a dynamical core only in two-dimensional cloud modeling. The extension into three dimensions of such a system has not been attempted to our knowledge. In this work, we establish a dynamical framework based on the vorticity equation for a three-dimensional anelastic cloud model.

The prognostic variables of the model are the two horizontal components of vorticity, potential temperature and mixing ratios of various phases of water at all levels, and the vertical component of vorticity at the model top. With the use of an expression for the nondivergence of the vector vorticity, the vertical component of vorticity at other levels is diagnostically determined. At the upper boundary, the uniform part of horizontal wind is predicted by the horizontally averaged equation of motion and the non-uniform part is obtained by solving the Poisson-type equations for streamfunction and velocity potential. Below the upper boundary, the horizontal wind is directly obtained from the predicted vorticity fields and the boundary values. For the vertical component of wind, a three-dimensional elliptic equation is solved with a prescribed vertical boundary

condition. This procedure replaces the elliptic equation for the perturbation pressure in the standard anelastic system based on the momentum equation, which produces computational complications when it is applied to flow over a complex terrain. Such complications are reduced in our system because the boundary conditions for the vertical velocity are more straightforward than those for perturbation pressure.

For advection of vorticity and scalar variables, the model has a flexibility to choose from a family of schemes by changing a single parameter, including a quadratically-conserving 2nd-order scheme, a quadratically-bounded 3rd-order scheme, and schemes in-between. The physical parameterizations in the model include a three-phase microphysical parameterization (Krueger et al. 1995; Lin et al., 1983; Lord et al. 1984), a radiative transfer parameterization (Fu et al. 1995), a surface flux parameterization (Deardorff, 1972), and a first-order turbulence closure that uses eddy viscosity and diffusivity coefficients depending on deformation and stability (Shutts and Gray, 1994). Except for the turbulence parameterization, these physical parameterizations are essentially the same as those in the two-dimensional cloud model originally developed by Krueger (1988), which has been applied to a variety of cloud regimes including stratocumulus, altocumulus, cumulo-nimbus and cirrus clouds (see, for example, Krueger 2000).

The three-dimensional cloud model based on the vorticity equation is first tested through idealized experiments simulating thermals in various environmental conditions. The main purpose of these experiments is to demonstrate the computational performance of the model as well as to gain understanding of some basic convective processes from the viewpoint of vorticity dynamics. To avoid unnecessary complications, these simulations are carried out with no physics. In the tests of the advection schemes, it is demonstrated that the 3^{rd}-order advection scheme effectively controls computational noise by keeping dispersion errors small. With that scheme, kinetic energy is practically conserved and potential enstrophy is bounded for axisymmetric flow. In the experiments designed to gain an insight into the interactions between three-dimensional motions associated with the convection, it is shown that the buoyant thermal under basic shear flow induces local wind

deceleration through the twisting effects on the vorticity components. This local wind deceleration is associated with the generation of a vertical vorticity couplet that has been reported in earlier studies. The budget analysis of vorticity also shows that advection is as important as the twisting effects in the distribution of the vorticity couplet.

The model is then tested with a simulation of ensemble clouds using the full model physics in a large domain. In this simulation, the initial thermodynamic state and horizontal wind fields are selected idealizing the GATE Phase-III conditions. Clouds are initiated by small random temperature perturbations. Large-scale forcing representing climatological background is imposed on the model through prescribed cooling and moistening rates. Preliminary results from this simulation are presented, showing development of mesoscale organization of clouds and modification of the mean flow by vorticity transports.

For future development of the current model, we are planning the following two modifications of the dynamical framework. The first modification is relaxing the computational constraint due to the anelastic approximation. In the current anelastic model, we solve a diagnostic equation for the vertical component of wind, which involves global calculations. Even with simple boundary conditions, the procedure to solve this equation can be a numerical burden, especially when the domain of the model is large. We believe that this problem can be overcome by relaxing the anelastic constraint even without introducing sound waves into the system. The second modification is to generalize the system of the anelastic equations while maintaining the structure of the model based on the three-dimensional vorticity equation. In its original form, the anelastic approximation requires that the reference state be isentropic (Ogura and Phillips, 1962). In practice, the reference state is usually taken to be nonisentropic. When the nonisentropic reference state is used, the full set of equations does not conserve energy in the system. To keep the energy conservation, modified anelastic systems have been proposed (Lipps and Hemler, 1982; Durran, 1989; Bannon, 1996). In our future efforts, we will focus on a generalization of the anelastic system without strong constraints by the choice of a reference state by generalizing the pseudo-incompressible approximation proposed by Durran (1989). We will also attempt to include full compressibility when linearized.

Acknowledgments. We wish to thank David Randall for constructive comments on the manuscript. This research is supported by the U. S. Department of Energy under Grant number DE-FG02-02ER63370 to Colorado State University and CSU Contract G-3816-3 to UCLA and by the National Aeronautics and Space Administration under Grant number NNG04GA76G to UCLA.

Reference

Arakawa, A., and V. R. Lamb, 1977: Computational design of the basic dynamical processes of the UCLA general circulation model. *Methods. Comput. Phys.*, **17**, 173–265.

Bannon, P., 1996: On the anelastic approximation for a compressible atmosphere. *J. Atmos. Sci.*, **53**, 3618–3628.

Cho, H. R. and T. L. Clark, 1981: A numerical investigation of the structure of vorticity fields associated with a deep convective cloud. *Mon. Wea. Rev.*, **109**, 1654–1670.

Cotton, W. R., G. Tripoli, R. Rauber and E. Mulvihill, 1986: Numerical simulation of the effects of varying ice crystal nucleation rates and aggregation processes on orographic snowfall. *J. Appl. Meteor.*, **25**, 1658-1680.

Deardorff, J. W., 1972: Parameterization of the planetary boundary layer for use in general circulation models. *Mon. Wea. Rev.*, **100**, 93–106.

Donner, L. J., C. J. Seman, R. S. Hemler, 1999: Three-dimensional cloud-system modeling of GATE Convection. *J. Atmos. Sci.*, **56**, 1885–1912.

Durran, D. R., 1989: Improving the anelastic approximation. *J. Atmos. Sci.*, **46**, 1453–1461.

Fu, Q., S. K. Krueger, and K. N. Liou, 1995: Interactions of radiation and convection in simulated tropical cloud clusters. *J. Atmos. Sci.*, **52**, 1310-1328.

Grabowski, W. W., X. Wu, M. W. Moncrieff, and W. D. Hall, 1998: Cloud-resolving modeling of cloud systems during phase III of GATE. Part II: Effects of resolution and the third spatial dimension. *J. Atmos. Sci.*, **55**, 3264–3282.

Johnson, D. E., P. K. Wang, and J. M. Straka, 1993: Numerical simulation of the 2 August 1981 CCOPE suppercell storm with and without ice microphysics. *J. Appl. Meteor.*, **32**, 745-759.

Khairoutdinov, M. F., D. A. Randall, 2003: Cloud resolving modeling of the ARM summer 1997 IOP: Model formulation, results, uncertainties, and sensitivities. *J. Atmos. Sci.*, **60**, 607–625.

Klemp, J. B., and R. B. Wilhelmson, 1978: The simulation of three-dimensional convective storm dynamics. *J. Atmos. Sci.*, **35**, 1070–1096.

Klemp, J. B., R. B. Wilhelmson, and P. S. Ray, 1981: Observed and numerically simulated structure of a mature supercell thunderstorm. *J. Atmos. Sci*., **38**, 1558-1580.

Krueger, S. K., 1988: Numerical simulation of tropical cumulus clouds and their interaction with the subcloud layer. *J. Atmos. Sci*., **45**, 2221-2250.

Krueger, S. K., 2000: Cloud system modeling. *General Circulation Model Development: Past, Present, and Future*, D. A. Randall Ed., Academic Press, 605-640.

Krueger, S. K., Q. Fu, K. N. Liou, and H.-N. Chin, 1995: Improvements of an ice-phase microphysics parameterization for use in numerical simulations of tropical convection. *J. Appl. Meteor*., **34**, 281-287.

Leslie, M. L. and G. S. Dietachmayer, 1997: Comparing schemes for integrating the Euler equations. *Mon. Wea. Rev*., **125**, 1687-1691.

Lin, Y.-L., R. D. Farley, and H. D. Orville, 1983: Bulk parameterization of the snow field in a cloud model. *J. Climate. Appl. Meteor*., **22**, 1065-1092.

Liou, K. N., Q. Fu, and T. P. Ackerman, 1988: A simple formulation of the delta-four-stream approximation for radiative transfer parameterizations. *J. Atmos. Sci*., **45**, 1940-1947.

Lipps, F. B., and R. S. Hemler, 1982: A scale analysis of deep moist convection and some related numerical calculations. *J. Atmos. Sci*., **39**, 2192–2210.

Lord, S. J., H. E. Willoughby and J. M. Piotrowicz, 1984: Role of a parameterized ice-phase microphysics in an axisymmetric, nonhydrostatic tropical cyclone model. *J. Atmos. Sci*., **41**, 2836-2848.

Mapes B. E., and X. Wu, 2001: Convective eddy momentum tendencies in long cloud-resolving model simulations. *J. Atmos. Sci*., **58**, 517–526.

McCumber, M., W. K. Tao, J. Simpson, R. Penc, and S. T. Soong, 1991: Comparison of ice-phase microphysical parameterization schemes using numerical simulations of tropical covection. *J. Appl. Meteo*., **30**, 985-1004.

Miller, M. J., and R. P. Pearce, 1974: A three-dimensional primitive equation model of cumulonimbus convection. *Quart. J. Roy. Meteor. Soc*., **100**, 133-154.

Moncrieff, M. W., and M. J. Miller, 1976: The dynamics and simulation of tropical cumulonimbus and squall lines. *Quart. J. Roy. Meteor. Soc*., **102**, 373-394.

Ogura, Y., and Phillips, N. A., 1962: Scale analysis of deep and shallow

convection in the atmosphere. *J. Atmos. Sci.*, **19**, 173–179.

Pastushkov, R. S., 1975: The effect of vertical wind shear on the evolution of convective clouds. *Quart. J. Roy. Meteor. Soc.*, **101**, 281-291.

Randall, D. A., 1994: Geostrophic adjustment and the finite-difference shallow-water equations. *Mon. Wea. Rev.*, **122,** 1371-1377.

Redelsperger, J.-L., P. R. A. Brown, F. Guichard, C. Hoff, M. Kawasima, S. Lang, T. Montmerle, K. Nakamura, K. Saito, C. Seman, W. K. Tao, and L. J. Donner, 2000: A GCSS model intercomparison for a tropical squall line observed during TOGA-COARE. I: Cloud-resolving models. *Q. J. R. Meteor. Soc.*, **126**, 823-863.

Rotunno, R., 1981: On the evolution of thunderstorm rotation. *Mon. Wea. Rev.*, **109,** 577-586.

Schlesinger, R. E., 1978: A three-dimensional numerical model of an isolated thunderstorm: Part I. Comparative experiments for variable ambient wind Shear. *J. Atmos. Sci.*, **35**, 690–713.

Schlesinger, R. E., 1980: A three-dimensional numerical model of an isolated thunderstorm. Part II: Dynamics of updraft splitting and mesovortex couplet evolution. *J. Atmos. Sci.*, **37**, 395–420.

Shutts, G. J. and M. E. B. Gray, 1994: A numerical modeling study of the geostrophic adjustment process following deep convection. *Q. J. R. Meteor. Soc.*, **120**, 1145-1178.

Simpson, J., G. VanHelvoirt and M. McCumber, 1982: Three-dimensional simulations of cumulus congestus clouds on GATE day 261. *J. Atmos. Sci.*, **39**, 126–145.

Smolarkiewicz, P. K., and T. L. Clark 1985: Numerical simulation of the evolution of a three-dimensional field of cumulus clouds. Part I: Model description, comparison with observations and sensitivity studies. *J. Atmos. Sci.*, **42**, 502–522.

Steiner, J. T., 1973: A three-dimensional model of cumulus cloud development. *J. Atmos. Sci.*, **30**, 414–435.

Sui, C.-H., and M. Yanai, 1986: Cumulus ensemble effects on the large-scale vorticity and momentum fields of GATE. Part I: Observational Evidence. *J. Atmos. Sci.*, **43**, 1618–1642.

Takacs, L. L., 1985: A two-step scheme for the advection equation with minimized dissipation and dispersion errors. *Mon. Wea. Rev.*, **113**, 1050–1065.

Tao, W.-K., and S.-T. Soong, 1986: A study of the response of deep tropical clouds to mesoscale processes: Three-dimensional numerical experiments. *J. Atmos. Sci.*, **43**, 2653–2676.

Tao, W.-K., J. Simpson, and S.-T. Soong, 1987: Statistical properties of a cloud ensemble: A numerical study. *J. Atmos. Sci.*, **44**, 3175–3187.

Tollerud, E. I. And S. K. Esbensen, 1983: An observational study of the upper-trpospheric vorticity fields in GATE cloud clusters. *Mon. Wea. Rev.*, **111**, 2161–2175.

Turpeinen, O. and M. K. Yau, 1981: Comparison of results from a three-dimensional cloud model with statistics of radar echoes on day 261 of GATE. *Mon. Wea. Rev.*, **109**, 1495–1511.

Wilhelmson, R. B., 1974: The life cycle of a thunderstorm in three dimensions. *J. Atmos. Sci.*, **31**, 1629–1651.

Wihelmson, R. B. and C. S. Chen, 1982: A simulation of the development of successive cells along a cloud outflow boundary. *J. Atmos. Sci.*, **39**, 1466-1483.

Wihelmson, R. B. and J. Klemp, 1978: A numerical study of storm splitting that leads to long-lived storms. *J. Atmos. Sci.*, **35**, 1974-1986.

Wihelmson, R. B. and J. Klemp, 1981: A three-dimensional numerical simulation of splitting severe storms on 3 April 1964. *J. Atmos. Sci.*, **38**, 1581-1600.

Xu, K.-M., and S. K. Krueger, 1991: Evaluation of cloudiness parameterizations using a cumulus ensemble model. *Mon. Wea. Rev.*, **119**, 342-367.

Zhang, G. J., and X. Wu, 2003: Convective momentum transport and perturbation pressure field from a cloud-resolving model simulation. *J. Atmos. Sci.*, **60**, 1120-1139.